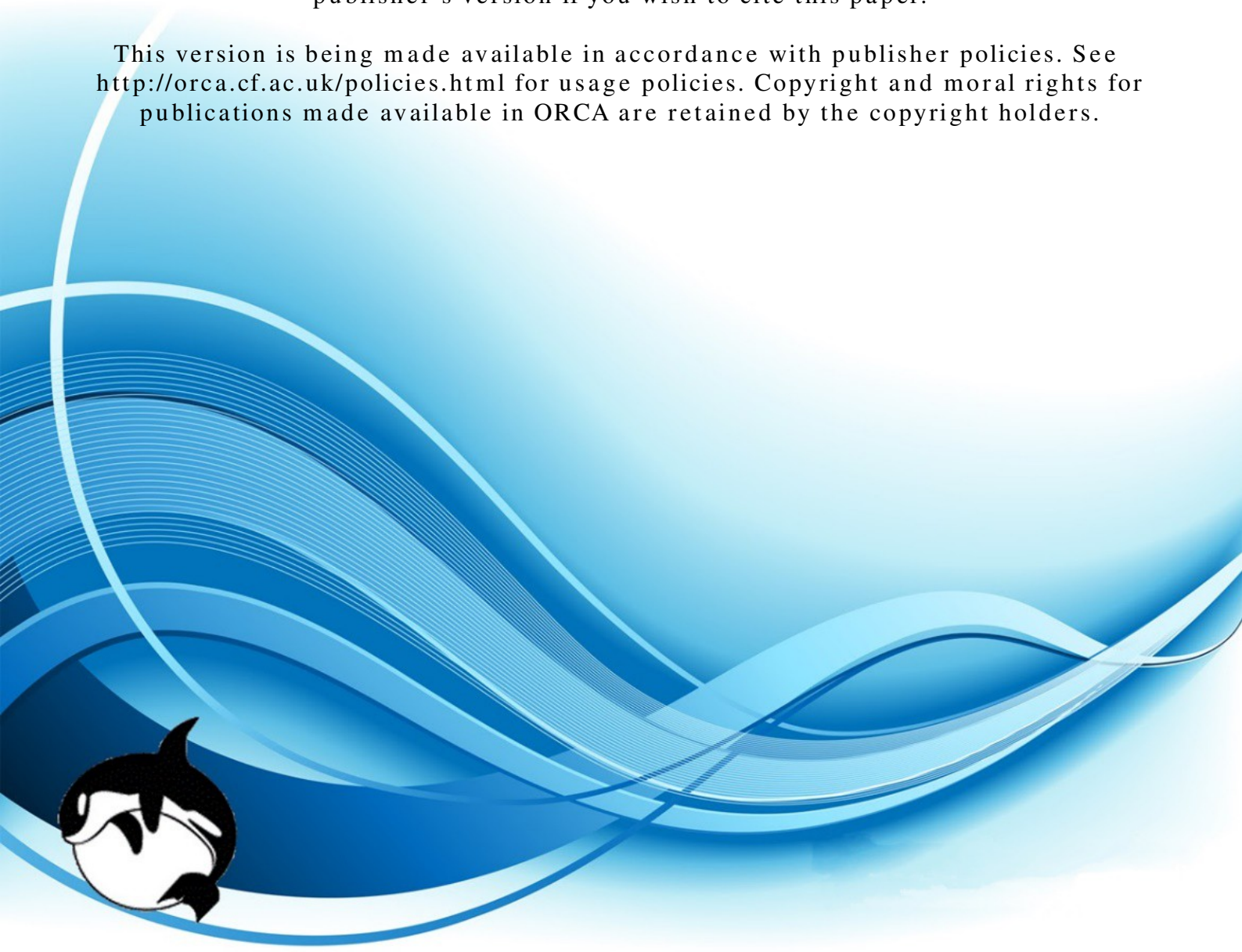

Corridors of crestal and radial faults linking salt diapirs in the Espírito Santo Basin, SE Brazil

Nathalia H. Mattos[1*] and Tiago M. Alves[1]

[1]3D Seismic Lab, School of Earth and Ocean Sciences, Cardiff University, Main Building-Park Place, CF10 3AT Cardiff, United Kingdom (mattosnh@cardiff.ac.uk)

Abstract

This work uses high-quality 3D seismic data to assess the geometry of fault families around salt diapir in SE Brazil (Espírito Santo Basin). It aims at evaluating the timings of fault growth, and suggests the generation of corridors for fluid migration linking discrete salt diapirs. Three salt diapirs, one salt ridge, and five fault families were identified based on their geometry and relative locations. Displacement-length (D-x) plots, Throw-depth (T-z) data and structural maps indicate that faults consist of multiple segments that were reactivated by dip-linkage following a preferential NE-SW direction. This style of reactivation and linkage is distinct from other sectors of the Espírito Santo Basin where the preferential mode of reactivation is by upwards vertical propagation. Reactivation of faults above a Mid-Eocene unconformity is also scarce in the study area. Conversely, two halokinetic episodes dated as Cretaceous and Paleogene are interpreted below a Mid-Eocene unconformity. This work is important as it recognises the juxtaposition of permeable strata across faults as marking the generation of fault corridors linking adjacent salt structures. In such a setting, fault modelling shows that fluid will migrate towards the shallower salt structures along the fault corridors first identified in this work.

Keywords: SE Brazil; Espírito Santo Basin; halokinesis; fault corridors; fluid flow.

1. Introduction

The investigation of subsurface faults and fractures is important in basin analysis as these structures play a crucial role in the entrapment and migration of fluids (Ainsworth, 2006; Bailey et al., 2002; Childs et al., 1997; Faulkner et al., 2010; Jolley et al., 2007; Knipe, 1997; Knipe et al., 1998; Walsh et al., 1998). Such a control of faults on fluid flow is particularly recorded in regions where the deposition of thick evaporite sequences is capable of influencing the structural styles of sedimentary basins (Brun and Fort,

2011; Hudec and Jackson, 2007; Smit et al., 2008; Stewart, 2006; Vendeville, 2002; Vendeville and Jackson, 1992). The movement of evaporite sequences through time (halokinesis) can result in the development of complex families of faults to form major structural compartments or, instead, promote the migration of fluids through reservoir and seal units (Alves et al., 2009; Carruthers et al., 2013; Fiduk et al., 2004; Gamboa et al., 2010; Jackson et al., 1994; Lohr et al., 2008; Stewart, 2006; Talbot et al., 1991). An early understanding of the mechanisms generating structural compartments in salt-rich basins can, therefore, increase the economic potential of new hydrocarbon prospects (Caine et al., 1996; Jolley et al., 2010, 2007; Knipe, 1997; Knipe et al., 1998).

The Espírito Santo Basin reveals a geological evolution that is similar to the Campos and Santos Basins, two of the most prolific hydrocarbon-bearing basins in SE Brazil (Bruhn et al., 2003; Chang et al., 1992; Cobbold et al., 2001; Demercian et al., 1993; Guardado et al., 2000; Guerra and Underhill, 2012; Meisling et al., 2001; Milani et al., 2001) (Fig. 1). Although being less known than its counterparts to the south, the Espírito Santo Basin hosts significant hydrocarbon accumulations in Cretaceous, Eocene-Oligocene and Miocene strata (Bruhn and Walker, 1997; Estrella et al., 1984; Fiduk et al., 2004; Katz and Mello, 2000). The Espírito Santo Basin also contains important volumes of evaporites, similarly to sedimentary basins in the Gulf of Mexico (Diegel et al., 1995; Rowan et al., 1999; Talbot, 1993), West Africa (Duval et al., 1992; Hudec and Jackson, 2002; Morley and Guerin, 1996) and Norway (Chand et al., 2008; Henriksen et al., 2011; Kane et al., 2010; Koyi et al., 1993). In the Espírito Santo Basin, halokinesis started in the Aptian–Albian and continued throughout the Cenozoic. It led to the development of discrete salt structures, and associated fault families, which were large enough to control the distribution and continuity of reservoir intervals in the Urucutuca Formation (Demercian et al., 1993; Fiduk et al., 2004) (Fig. 2). Hence, the structural framework of the Espírito Santo Basin comprises horsts and grabens below and Aptian evaporite unit, and supra-salt structures such as diapirs, salt rollers and rollovers, turtle anticlines, rafts and salt walls (Alves, 2012; Fiduk et al., 2004; Varela and Mohriak, 2013) (Figs. 2 and 3).

The aim of this paper is to describe the geometry and character of faults formed adjacently to three salt diapirs, and on the crest of a buried salt ridge, herein named as Salt Ridge (Fig. 4). We investigate the timing of formation of salt-related faults to conclude if they form at present, or formed in the past, structural corridors connecting distinct salt structures. The controls exerted by these fault corridors on

fluid flow and strata compartmentalisation, under different stress regime(s), are assessed in detail. In summary, we aim at addressing the following research questions:

a) How does halokinesis influence fault families developed close to salt structures?

b) Are there any preferred directions to the reactivation of faults in the study area?

c) Is there a relationship between fault reactivation and the migration (or trapping) of fluids around salt structures?

d) How can the studied diapir systems provide insights into the evolution of the Espírito Santo Basin, contributing to the analysis of seal competence (and fluid migration) in the areas where halokinesis plays a central role?

This study is the first to determine a paleostress tensor for the Espírito Santo Basin, to model slip tendency and leakage factors for the interpreted faults, and to create juxtaposition diagrams to assess where fluids were more likely to migrate along (or across) faults. In the discussion section, an evolutionary model is proposed for the interpreted salt structures and related faults. This model addresses the timing(s) and relationship(s) between different fault families. The reasons for localised fault reactivation are also investigated and discussed in light of published work on different parts of the Espírito Santo Basin (e.g. Baudon and Cartwright, 2008; Omosanya and Alves, 2013; Ze and Alves, 2016). At the end of this paper, our results, and the integrated effects of halokinesis on the trapping and migration of fluids, are compared to areas with similar halokinetic structures.

2. Geological Setting

The Espírito Santo Basin comprises a rift basin developed in SE Brazil during the Late Jurassic-Cretaceous (Fig. 1). The basin covers an offshore area of ~ 200,000 km^2, while its continental part reaches 18,000 km^2 (Mohriak, 2003). Its northern limit is the Abrolhos Bank, a Paleogene volcanic plateau that separates Espírito Santo from the Cumuruxatiba Basin (Mohriak, 2005). The Vitória-Trindade High separates the Espírito Santo Basin from the Campos Basin to the south (França et al., 2007) (Fig. 1).

The tectono-sedimentary history of the Espírito Santo Basin comprises four evolution stages: pre-rift, syn-rift, transitional and drift (Cobbold et al., 2001; Ojeda, 1982). These four stages correlate with five

depositional megasequences: pre-rift, rift, transitional, transgressive-marine and regressive-marine (Fiduk et al., 2004; Mohriak et al., 2008) (Fig. 3).

The pre-rift stage (Late Jurassic – Early Cretaceous) is associated with the Serra Geral magmatic event, which was initiated in the Paraná Basin and later reached areas of the continental margin such as the Espírito Santo Basin (Cainelli and Mohriak, 1999; Mohriak, 2003).

The syn-rift stage (Late Barresian - Early Aptian) is characterised by intense tectonism and corresponding formation of the East Brazil Rift System in response to divergent motion between South America and Africa (Chang et al., 1992; Demercian et al., 1993; França et al., 2007; Ojeda, 1982). In the syn-rift megasequence three main depositional systems were accumulated in narrow, fault-controlled depocentres generated between Espírito Santo and the Sergipe/Alagoas Basins to the north: 1) alluvial fans, fan deltas and transitional deposits, 2) lacustrine shales and marls, and 3) lacustrine pelecypod limestones (*coquinas*) (Cainelli and Mohriak, 1998). In the study area, the syn-rift megasequence is represented by the Cricaré Formation (Fig. 2; França et al., 2007; Vieira et al., 1994).

The end of continental rifting marks a transitional phase in the Espírito Santo Basin (Mohriak, 2003; Ojeda, 1982). The formation of a narrow and elongated basin, in an arid climate with little water circulation, promoted the accumulation of a thick evaporite megasequence during the Aptian (Mariricu Formation; Fig. 2). This megasequence forms the main seal unit above syn-rift strata (Chang et al., 1992; Demercian et al., 1993; França et al., 2007; Mohriak, 2003; Ojeda, 1982).

During the Late Cretaceous - Holocene drift stage, continuous subsidence resulted in the development of an open-marine setting (Bruhn and Walker, 1997; Cainelli and Mohriak, 1999; Mohriak, 2003). During the drift stage, the evaporitic (transitional) megasequence changed gradually into marine strata (Cainelli and Mohriak, 1998), and two megasequences were subsequently formed: the Early Drift Transgressive megasequence (Albian to Ypresian), consisting of dark shales, turbiditic sandstones and carbonate breccias from the Urucutuca Formation (Cainelli and Mohriak, 1998; França et al., 2007), and the Late Drift Regressive megasequence (Lutetian – Holocene), which comprises mixed siliciclastic and volcaniclastic units resulting from the erosion of the Serra do Mar and Serra da Mantiqueira mountains. Erosion of coastal mountain ranges occurred together with tectonic uplift and local volcanism on the Abrolhos Bank (Figueiredo and Mohriak, 1984; França et al., 2007; Mohriak, 2003) (Fig. 3). As a result, the volcaniclastic Abrolhos Formation became interbedded with thick turbidite intervals in the Urucutuca Formation during the late drift stage, particularly within channelised bodies whose distribution was

117 controlled by halokinesis (Cainelli and Mohriak, 1998; Figueiredo and Mohriak, 1984; França et al.,
118 2007; Mohriak, 2003) (Fig. 2).

119 Halokinesis, and the subsequent development of salt structures in the Espírito Santo Basin, was
120 initiated in the Late Aptian-Early Albian in response to differential loading, gravity spreading and
121 downslope thin-skinned gravitational gliding above Aptian evaporites (Demercian et al., 1993; Fiduk et
122 al., 2004). Halokinesis generated structures such as salt pillows, salt rollers, vertical salt diapirs with
123 overhangs, allochthonous salt tongues along contractional folds, salt canopies and tongues, turtle
124 structures and large salt nappes (Fiduk et al., 2004; Strozyk et al., 2017) (Fig. 3). In the Espírito Santo
125 Basin, the growth of salt structures continued through the Cenozoic as a result of: a) continued sediment
126 transport onto the continental slope, and b) regional magmatism associated with the Abrolhos Plateau,
127 two phenomena that resulted in continuous growth and deformation of pre-existent salt structures (Fiduk
128 et al., 2004).

129 The study area is characterised by the occurrence of salt diapirs (Fig. 4). Post-salt strata were
130 deformed by halokinesis during the Cenozoic (Alves, 2012; Alves et al., 2009; Baudon and Cartwright,
131 2008a), in association with three phases of fault growth (Baudon and Cartwright, 2008a; Omosanya and
132 Alves, 2014). Halokinesis also resulted in the accumulation of thick, vertically stacked mass-transport
133 deposits (MTDs) during the Middle Eocene - Early Miocene (Fiduk et al., 2004; Gamboa et al., 2010;
134 Omosanya and Alves, 2013).
135

136 **3. Data and methods**

137 The interpreted 3D seismic volume covers an area of 1,670 km^2 within the Espírito Santo Basin, at a
138 water depth ranging from 100 m to 1800 m (Fig. 1). The seismic data were pre-stacked time migrated
139 with a 12.5 x 12.5 m grid line spacing, and acquired with a 6 x 5.700 m array of streamers. The data were
140 processed in the time domain and zero-phased within a 2 ms vertical sampling window. Resampling at 4
141 ms with the application of anti-aliasing filter, TAU-P linear noise attenuation and TAU-P domain
142 deconvolution preceded data processing. Three-dimensional pre-stack time migration used the Kirchhoff
143 algorithm.

144 In this work, seismic data are displayed using the standard SEG convention for a zero-phase wavelet;
145 an increase in acoustic impedance is shown as a red seismic reflection and a relative decrease in acoustic
146 impedance is shown in blue. The vertical extent of the seismic survey is limited to 4.0 s Two-way travel

147 time (TWTT). Average p-wave velocity data from Deep Sea Drilling Project (DSDP) Site 516 (Barker et
148 al., 1983), located in the Santos Basin (Fig. 1), show values of 3100 m/s for the Late Cretaceous -
149 Paleocene interval, and 2100 m/s and 1800 m/s for Eocene-Oligocene and Miocene-Holocene strata,
150 respectively. These velocities were used to convert mapped faults and horizons to depth, and to obtain the
151 true dip of faults. Based on the velocities for the DSDP Site 516, and a computed dominant frequency of
152 40 Hz, the vertical resolution of the seismic data was also estimated for distinct intervals. Considering a
153 resolution limit of ¼ of the wavelength (λ) (Sheriff and Geldart, 1995), the Late Cretaceous – Paleocene
154 interval has a vertical resolution of ~19 m, whereas the Eocene-Oligocene and the Miocene-Holocene
155 intervals have vertical resolutions of ~13 m and ~11 m, respectively.
156 Ten (10) key seismic reflections, including the seafloor, were mapped in this work at a spacing of ten
157 lines (125 m). Smaller intervals of 1-5 lines (12.5 to 62.5 m) were used to map salt diapirs as discrete
158 structures. Based on the published DSDP well data for SE Brazil, published seismic-stratigraphic
159 frameworks (Alves et al., 2009; Fiduk et al., 2004; Gamboa et al., 2012; Gamboa and Alves, 2015; Viana
160 et al., 2003), and the character and geometry of the interpreted seismic reflections, we defined three
161 principal units in the study area: Late Cretaceous – Paleocene (Unit 1), Eocene – Oligocene (Unit 2), and
162 Miocene – Quaternary (Unit 3). (Fig. 3, Table 1). Structural maps of horizons H_1, representing the top-salt
163 horizon, and H_6 (corresponding to the Mid-Eocene unconformity that bounds Unit 1 at the top), are
164 shown in this paper (Fig. 5).
165
166 *3.1. Structural analyses*

167 Variance time-slices were used to map distinct fault families around salt structures based on their
168 geometry, orientations, and relationship with main structural features. Variance data are computed by
169 converting a seismic-amplitude volume into a discontinuity volume, thus highlighting the most prominent
170 discontinuities in a 3D seismic volume, including faults and fractures (Brown, 2011).
171 Two hundred and fifteen (215) faults were manually mapped every inline (12.5 m), and every five
172 crosslines (62.5 m). The mechanisms of initiation, growth, and propagation of faults can be depicted
173 using displacement data (e.g. Baudon and Cartwright, 2008; Cartwright and Mansfield, 1998). In detail,
174 the relationship between the maximum displacement (D_{max}) and the length (x) of a fault trace is the basis
175 for displacement-length (D-x) analyses (Cowie and Scholz, 1992; Muraoka and Kamata, 1983; Nicol et
176 al., 2002; Peacock and Sanderson, 1991). In this work, displacement was measured for twelve (12)

177 representative faults at a pre-defined cut-off horizon. Displacement and distance data, originally in ms
178 TWTT, were converted into metres. Plots of maximum displacement (D_{max}) against length (x), compiled
179 for all faults in the study area, were then compared to published data (e.g. Muraoka and Kamata, 1983;
180 Scholz and Cowie, 1990; Walsh et al., 2002; Walsh and Watterson, 1987) for normal, strike-slip and
181 reverse faults using the *Fault Analysis Module* in Midland Valley Move®.

182 The relationship between fault throw (T) and depth (z) is widely used to estimate fault reactivation
183 (Baudon and Cartwright, 2008a, 2008b; Cartwright and Mansfield, 1998; Mansfield and Cartwright,
184 1996). Throw-depth (T-z) profiles for reactivated faults show abrupt variations in throw gradient and
185 values, whereas minor changes (and comparatively smaller throw values) are obtained for non-reactivated
186 faults (Baudon and Cartwright, 2008a). In this work, we show throw-depth relationships for the 12
187 representative faults previously mentioned using seismic profiles that are orthogonal to the fault strikes,
188 and measuring the vertical offset between hanging-wall and footwall cut-offs (Baudon and Cartwright,
189 2008a; Mansfield and Cartwright, 1996; Mattos et al., 2016; Omosanya and Alves, 2014). The resulting
190 T-z profiles were created in Microsoft® Excel, with values displayed in two-way travel time (ms TWTT).

191 Displacement analyses were carried out so that faults and horizons interpreted in Petrel® could be
192 imported into Midland Valley Move® as 3D mesh surfaces, and later filtered for edge triangles. Key fault
193 attributes, including true dip, strike and azimuth for each fault vertex, were created in Move® using the
194 *Attribute Analyser Toolbar*. Fault analyses performed in this paper included the creation of juxtaposition
195 diagrams and stress analyses.

196 Stratigraphic juxtaposition is a widely-applied method to predict the potential of fluid retention and
197 migration through faults (Allan, 1989; Knipe, 1997; Reilly et al., 2016). The juxtaposition of
198 impermeable strata, such as shales, against permeable units (sandstones), can create an effective seal. In
199 contrast, the juxtaposition of permeable units is likely to promote cross-fault lateral migration. We used
200 the *Fault Analysis Module in Move®* to create hanging-wall and footwall cut-off lines for
201 stratigraphically-assigned seismic horizons using a trim distance of 15 m. Juxtaposition diagrams (Allan
202 diagrams) were created for the 12 representative faults considered in this work.

203 Stress analyses were performed to assess the orientation and distribution of the principal paleostress
204 tensors associated with the 12 representative faults using the *Stress Analysis Module* in Move®. The
205 paleostress inversion method is based on the relationship between slip-tendency values and displacement
206 measured for a set of faults (McFarland et al., 2012). Fault slip tends to occur if shear stress is equal or

greater than the normal stress acting on a fault surface (Morris et al., 1996). Two important criteria must be taken into account when assessing the inverted stress tensor: a) a positive relationship between the slip tendency and displacement is expected, and b) surfaces with high slip tendency and large displacements indicate an early slip, whereas small displacements indicate that the fault slip started at a later time (McFarland et al., 2012). Once we obtained the paleostress azimuths and magnitudes, we modelled the slip tendency and the leakage factor using the *Stress Analysis Module* for the faults in the study area.

Slip tendency (T_s) is defined as the likelihood of a fault to slip, and is estimated as the ratio of shear (τ) to normal (σ_n) stresses on a fault plane (Equation. 1; Morris et al., 1996). Slip tendency has no units and is mathematically written as:

$$T_s = \frac{\tau}{\sigma_n'}$$

Eq. (1)

Slip tendency is dependent on the orientation of a fault surface and the stress field acting on it. A fault will slip according to the cohesive strength of its surface, and the coefficient of static friction (μ). Slip for a cohesionless fault surface will occur when the resolved shear stress is equal or exceeds the frictional resistance to sliding (F), as shown in Equation 2 (Morris et al., 1996):

$$F \leq \tau = \mu\sigma_n$$

Eq. (2)

The fluid transmissivity of faults can be modelled by estimating a Leakage factor (L). Faults that either constitute migration conduits for fluids in the subsurface, or act as local seals, can be estimated quantitatively on colour-scaled 3D maps of fault planes. Leakage factor is defined as the ratio of the fluid pressure (P_f) to the difference between the normal stress (σ_n') and the tensile strength (T) of a fault zone (Equation. 3; Morris et al., 1996) such as:

$$L = P_f/(\sigma_n' - T)$$

Eq. (3)

The magnitudes and azimuths obtained from our paleostress analysis were used together with a fluid pressure (P_f) value of 9 MPa, obtained from the locally estimated vertical stress, and considering both the depth of the unit of interest and the water column above the seafloor (Zoback, 2010).

Fault reactivation must be taken into account when assessing the leakage potential of a reservoir interval. Methods to assess the risk of breaching seal units by the juxtaposition of permeable strata across faults include detailed assessments of fault geometry and the use of in-situ stresses (Ferrill et al., 2009; Jones and Hillis, 2003; Morris et al., 1996). However, the absence of borehole breakout data for the Espírito Santo Basin made necessary the use of paleostress data, and juxtaposition diagrams, to provide evidence for reservoir compartmentalisation associated with fault reactivation.

4. Seismic stratigraphy of the Espírito Santo Basin

4.1. Unit 1 (Albian– Middle Eocene)

Unit 1 is the primary unit of interest in this paper (Figs. 4 and 6 to 8). Unit 1 comprises sub-units 1a to 1e. It is bounded at its base by horizon H_1 and at its top by a Mid-Eocene unconformity defined by horizon H_6 (Figs. 4 and 6 to 8). Sub-unit 1a is bounded at its base by horizon H_1 (Figs. 4 and 6 to 8), a moderate- to high-amplitude negative reflection, and at its top by the moderate-amplitude (and nearly continuous) horizon H_2 (Figs. 4 and 6 to 8). Low-amplitude to transparent seismic reflections predominate in this sub-unit. Its thickness ranges between 200 – 500 ms, decreasing on the flanks of salt structures. Sub-unit 1a is likely composed of distal turbidites and shale-rich carbonates (Alves et al., 2009; Fiduk et al., 2004; Viana et al., 2003).

Horizon H_2 delimits the base of sub-unit 1b. The upper boundary of this 75 ms- to 175 ms-thick sub-unit is defined by horizon H_3 (Figs. 4 and 6 to 8). The sub-unit is offset by faults that are radial to the smaller salt diapirs, and by faults developed on the Salt Ridge (Figs. 4 and 6 to 8). The internal character of sub-unit 1b becomes chaotic in the proximity of the Rio Doce Canyon System (Fig. 4). In the area of interest to this study, sub-unit 1b is characterised by moderate-amplitude, sub-parallel seismic reflections that reflect an increase in sand volume relative to sub-unit 1a.

Sub-unit 1c is defined at its base by horizon H_3 and at its top by horizon H_4 (Figs. 4 and 6 to 8). This sub-unit consists of a 25 ms-thick, moderate amplitude package interpreted as shale. Horizon H_4 delimits the base of Sub-unit 1d, which comprises a 40 ms-thick package with moderate amplitude. The amplitude of this sub-unit increases close to diapirs and salt-ridge crests due to a relative increase in sand content.

Horizon H_5 delimits the base of sub-unit 1e, a 75 ms- to 175 ms-thick package delimited at its top by a regional erosional unconformity; horizon H_6 (Figs. 4 and 6 to 8). Sub-unit 1e comprises transparent to low-amplitude internal reflections, which become chaotic close to diapirs and the Rio Doce Canyon System. This sub-unit is likely composed of fine-grained (clayey) turbidites. Close to the Rio Doce Canyon System, these fine-grained units alternate with sand-rich turbidites (Alves et al., 2009; Viana et al., 2003). The majority of faults in the study area are truncated by horizon H_6 at their upper tips (Figs. 4 and 6 to 8).

4.2. Unit 2 (Middle Eocene – Early Miocene)

Unit 2 is delimited at its base by a Mid-Eocene unconformity, horizon H_6 (Fig. 5b). Faulting is ubiquitous at this level, but rarely propagates into the upper part of Unit 2 (Figs. 4 and 6 to 8). Unit 2 consists of chaotic low-amplitude to transparent reflections intercalated with moderate amplitude strata. The base of Unit 2 (sub-unit 2a) is characterised by blocky mass-transport deposits (MTDs) accumulated around a buried salt ridge developed between diapirs D1 and D2 (Gamboa and Alves, 2015). Blocks are moderate-amplitude features with sharp to smooth edges (Figs. 4 and 6 to 8). The middle and upper parts (sub-units 2b and 2c) of Unit 2 are characterised by the occurrence of high-amplitude seismic reflections previously interpreted as sand-rich turbidite lobes (Alves et al., 2009; Gamboa and Alves, 2015). These two sub-units are separated by horizons H_7 and H_8 (Figs. 4 and 6 to 8). The upper boundary of Unit 2 is defined by the Early Miocene horizon H_9 (Figs. 4 and 6 to 8).

4.3. Unit 3 (Miocene – Quaternary)

The base of Unit 3 coincides with Horizon H_9, whereas the sea floor delimits its top. Unit 3 is characterised by low-amplitude, sub-parallel seismic reflections incised by submarine channels (Figs. 4 and 6 to 8). Submarine channels are deformed close to salt diapirs (Figs. 4 and 6 to 8). Unit 3 includes interbedded sand, shale-rich turbidites and hemipelagic sediment (Fiduk et al., 2004; Viana et al., 2003).

5. Fault distribution around salt structures

292 In agreement with previous work by Fiduk et al. (2004), Gamboa, (2011) and Gamboa and Alves
293 (2015), we interpret the salt structures in the studied area as rooted on the NW-trending Salt Ridge. This
294 Salt Ridge shows a maximum width of ~ 2.7 km and a length of 10 km, merging at depth with diapir D1.
295 The Salt Ridge forms an anticlinal structure with a lenticular shape (Figs. 6a and 6b). In contrast to
296 adjacent salt structures, Units 1 to 3 bury the Salt Ridge and faults are well developed on the crest of this
297 structure.
298 Diapir D1, located in the eastern part of the study area, has a diameter of ~ 5.4 km (Fig. 8). Diapir
299 D1 penetrates the post-salt overburden to a depth ~ 400 ms below the sea floor, deforming Units 1 to 3
300 (Fig. 8). Diapir D2 shows a diameter of 2.6 km and is the smallest diapir in the study area. It penetrates
301 through Units 1 and 2 and partially through Unit 3 (Fig. 7). Diapir D3 occurs in the NW part of the study
302 area and shows a diameter of ~ 7.1 km. Over diapir D3, salt has deformed the three stratigraphic units to
303 reach the sea floor (Fig. 6a).
304 Structural interpretations based on the analysis of seismic profiles (Figs. 4 and 6 to 8) combined with
305 variance time-slices (Fig. 9) allowed us to subdivide the imaged faults into five (5) families based on their
306 position relative to the principal salt ridge and adjacent diapirs.
307
308 *5.1. Faults on the Salt Ridge*

309 The preferential trend for the 55 faults mapped over the buried Salt Ridge is NW-SE (Fig. 10a). This
310 trend corresponds to 72% of the faults developed on the ridge, including F1 and F12 (Fig. 10a). The NW-
311 striking faults in the Salt Ridge are longer than their NE-striking counterparts (Fig. 9). The average length
312 of the faults in the salt ridge is 1.2 km. Faults dip both to the NE and SW (Fig. 10a).
313 One of the most distinctive features of this family of faults is the occurrence of fault F1, the largest
314 in the study area, with a length of 9.5 km. Fault F1 is parallel to the salt ridge and terminates to the NE of
315 diapir D1 (Fig. 9). Fault 12 occurs to the north of D1. Faults F1 and F12 follow the same direction of the
316 Salt Ridge and are confined to Unit 1, with no evidence of faults reaching the MTDs in Unit 2 (Figs. 6a
317 and 6b). Tilt blocks formed at the crest of the buried ridge do not show growth strata on the seismic
318 sections (Figs. 6a and 6b). Distinctive bright reflections occur between -3280 and -3420 ms, in Sub-Unit
319 1c (Fig. 6b).
320
321 *5.2. Diapir 1 (D1)*

322 Fifty-three (53) faults were mapped around diapir D1 to show a radial distribution (Fig. 9).
323 Approximately 57% of the mapped faults have a NW trend over D1, whereas the remaining 43% trend to
324 the NNE (Fig. 10b). Faults around D1 dip preferentially to the NE, showing an average dip of 32º.
325 Representative faults include F2, F3, F8 and F9 (Fig. 9). Most faults occur between horizons H_2 and H_6.
326 However, an important number of faults also offset horizon H_1, including F2 and F9 (Fig. 6b).
327 One of the most striking features around D1 is fault F3, a NW-trending structure with an average dip
328 of 41º, offsetting horizons H_2 to H_9 along its length (Fig. 7). Fault F2 is NNE-striking, terminating against
329 the Salt Ridge. A sucession of tilt-blocks is observed on the crest of D3 (Figs. 8a and 8b) and radially to
330 D1 (Fig. 8a). Radial faults include fault F9, a 3.3-km long NW-striking structure that extends towards D3
331 (Fig. 9). Next to D1, NW-striking faults occur and bright reflections are observed in strata offset by fault
332 F8 (Fig. 8a).
333
334 *5.3. Southern area*

335 The southern part of the study area is the most faulted in the study area, with 77 faults (Fig. 9). Here,
336 faults do not have a radial distribution; the preferential orientation is NW-SE for 36% of these faults,
337 while the least common strike is to the SW for 19.7% of the faults (Fig. 10c). By comparing the faults
338 mapped in the southern area with those around the salt diapirs we observe that the former are smaller in
339 length (average length 0.8 km) and limited to Unit 1 (Fig. 8). Some of the faults propagate from the
340 Aptian salt, reaching depths of -3880 ms. However, none of the faults offset the Mid-Eocene
341 unconformity (horizon H_6) or extend into Unit 2 (Fig. 8). On the variance maps, faults mapped in the
342 southern part have polygonal distributions (Fig. 9). The southern area shows a greater concentration of
343 bright reflections along fault blocks compared to other parts of the seismic volume (Figs. 8a and 8b).
344
345 *5.4. Diapir 2 (D2)*

346 Eleven (11) faults were mapped around diapir D2, and data plotted on the rose diagram in Figure
347 10d, show a radial distribution with 75% of the faults varying in strike between 180º and 360º. The
348 average dip for these faults approaches 30º. Although most of these faults are observed in Unit 1, some
349 structures close to D2 (including fault F7) offset the top of the Aptian salt (horizon H_1) and terminate in

sub-unit 2b (Figs. 7 and 8b). Away from D2, the NE-striking fault F7 offsets horizons H_2 to H_5 (Fig. 7). A bright reflection occurs close to diapir D2, on the footwall of fault F6 (Fig. 7).

5.5. Diapir 3 (D3)

Nineteen (19) faults were mapped around diapir D3, and show a radial distribution (Fig. 9). Approximately 46% of the faults strike to the NW, and 22% of the faults strike to the SW (Fig. 10). Faults radial to D3 include both synthetic and antithetic faults (Fig. 8). Most of the faults occur between horizons H_2 and H_6, on the crest of D3, and rarely offset horizon H_1. A distinctive feature around D3 is the occurrence of faults offsetting the base of MTDs in sub-unit 2a (Figs. 6b, 8a and 8b). The average length for this group of faults is 1.6 km, with representative faults F10 and F11 striking to the NW (Fig. 9). Bright reflections are observed close to faults radial to D3 (Fig. 8). A large number of bright reflections are also found above faults in Unit 2 (Figs. 6b, 8a and 8b).

6. Fault displacement analysis

6.1. Interpretation of distance-length (D-x) profiles

Displacement-length (D-x) plots were compiled for the twelve (12) representative faults using horizon H_5 as reference (Fig. 11). The geometry of the D-x profiles relates to the observed displacement variations along the total length of a fault. For single and isolated faults, D-x profiles represent a near-symmetric slope with gentle variations in displacement and flat-topped curves, which are characteristic of C-type faults (Childs et al., 1995; Muraoka and Kamata, 1983; Nicol et al., 1996; Peacock and Sanderson, 1991). Complex D-x profiles result from the presence of abrupt variations in displacement along faults, a character indicating linkage of individual fault segments associated with displacement minima during fault growth (Walsh et al., 2003). These structures are classified as M-Type faults (Muraoka and Kamata, 1983), and their characteristic profiles show a broad central section with no significant slope variations. Their tips show abrupt displacement variations, resulting in a marked asymmetric character on D-x plots. Displacement maxima relate to the first nucleation point for individual fault segments (Barnett et al., 1987; Nicol et al., 1996; Walsh and Watterson, 1987). This assertion, however, is only true for non-segmented or isolated blind faults.

379 Overall, the geometry of the D-x profiles varies from asymmetric (F1, F5, F6, F7, F9, F10 and F11)
380 to symmetric (F2, F3, F4, F8, and F12). Faults F3 and F4 have distinctive M-type profiles. In detail, F5 is
381 skewed to the east, whereas F6 is skewed to the northwest. The remaining faults have more complicated
382 displacement profiles. Faults F4 and F7 for example, are a combination of C-type profiles on the left (NE
383 and W, respectively) and an M-type profiles on their right (SW and E, respectively) (Fig. 11). Faults F6,
384 F7, F8 and F10 terminate at the edge of the salt diapir, and no nil displacements values were observed at
385 such point (Fig. 11). Two near-flat profiles seem to be the preferential D-x geometry for fault F9. Faults
386 F1, F11 and F12 have the most complex displacement profile, with a succession of several C-, M-, and
387 skewed-type profiles (Fig. 11).
388 Fault geometries are more complex around the Salt Ridge and D3 when compared to the remainder
389 of the study area. The complexity of these D-x profiles indicates that faults formed around salt structures
390 were not fully isolated during their propagation and growth. However, the presence of displacement
391 minima indicate that fault development in the study area is a combination of initially isolated fault
392 segments, which grew laterally to a maximum length to become constant-length faults (*cf.* Childs et al.,
393 1995; Peacock and Sanderson, 1991). Fault F2 is the only fault in the study area with an overall shape
394 resembling the C-type profile of Muraoka and Kamata (1983).
395 A relationship between fault segmentation and fault length can be established considering that large
396 faults such as F1 (9.5 km), F11 (5.5 km) and F12 (3.8 km), appear to be the most segmented structures in
397 the study area. They show clear displacement minima, whereas in small faults such as F4 (1.4 km) and F8
398 (750 m), variations in displacement seem to be less significant. For the remaining faults, the number of
399 segments varies with fault length at different scales. In addition to fault segmentation, representative
400 faults also have variable maximum displacement (d_{max}) and fault length (Fig. 11). Values of D_{max} range
401 from 82.83 m (F1) to 36.75 m (F8), while fault length varies from about 750 m (F8) to 9.5 km (F1).
402
403 *6.2. Interpretation of throw-depth (T-z) profiles*

404 Throw-depth (T-z) plots for the 12 representative faults are shown in Fig. 12. Throw profiles in the
405 study area include M- (F1, F2, F6, F9) and C-types (F4, F5) *cf.* Muraoka and Kamata (1983). Fault F3 is
406 an example of a skewed M-type profile. Often, the T-z profiles of some faults show a hybrid character
407 that results in the combination of two or more throw profiles. Fault F7 consists of a combination of M-
408 and C-types in Unit 1, whereas an M-type profile is observed in Units 2 and 3. The throw profiles for

faults F10 and F12 show a combination of M- and C-types profiles. Faults F8 and F11 consist of two M-type profiles (Fig. 12).

Throw minima and maxima vary significantly across seismic horizons and at depth. The position of throw minima and maxima across stratigraphic levels appears to relate to fault segmentation and reactivation by dip-linkage (Baudon and Cartwright, 2008a; Omosanya and Alves, 2014; Walsh and Watterson, 1989). For faults F2, F4, F9, F10, F11 and F12, a significant reduction in throw values occurs at horizon H_2 (Fig. 12). Faults F1, F6, F7 and F8 show distinct throw minima within sub-unit 1a. A second negative displacement is recorded close, or at horizon H_5, for faults F1, F3, F5, F7, F8, F11 and F12. Throw maxima occur at sub-unit 1e, delimited by horizons H_5 and H_6, for faults F2, F3, F6, F7, F9, F10 and F12, while for fault F1 maximum throw occurs at horizon H_5 (Fig. 12). The position of the throw maxima in the analysed faults implies nucleation of the faults in sub-unit 1e.

The maximum throw recorded for the faults in the study area is 50 ms for fault F5. Compared to the other faults, F8 show a distinct throw profile, characterised by small throw values close to the upper tips of the fault and increase with depth, whereas the majority of the faults seem to show a relative decrease i with depth.

Displacement ideally decreases to zero towards fault tips, a character reflecting their propagation towards a free surface, and increases to a maximum in the centre of the fault surface (Childs et al., 2003; Kim and Sanderson, 2005; Walsh and Watterson, 1988). However, most of the faults in the study area show significant displacement on their upper tips, reflecting near-sea floor erosion at the time of their propagation. The faults studied in this paper are truncated by the Mid-Eocene unconformity (horizon H_6) on the seismic sections (Figs. 3 and 6 to 8). Exceptions to this pattern include faults F3 and F7, both propagating above the Mid-Eocene unconformity and reaching Unit 3. For fault F3, its upper tip is truncated by a submarine channel in Unit 3 (Fig. 7). The T-z profiles for these two faults show an abrupt displacement shift to the left at the horizon H_6 (Fig. 12), followed by an increase in throw at shallow levels, indicating the occurrence of a reactivation episode. Considering that faults F3 and F7 are located adjacent to diapirs D2 and D3, it is possible to suggest that fault reactivation occurred in response to the growth of these salt structures. Halokinesis did not affect the upwards propagation of other faults in the study area, as they chiefly terminate at the base of the MTDs in Unit 2, i.e. below the Mid-Eocene horizon H_6 (Fig. 12).

7. Stratigraphic juxtaposition

The displacement of permeable and impermeable units across fault planes can be graphically represented by Allan Diagrams (Allan, 1989). Juxtaposition (Allan) diagrams were created for faults F1 to F12 by assigning stratigraphic intervals as salt, limestone, shale, silt and sand to the interpreted seismic units and sub-units (Fig. 13). In the salt ridge, we estimate the juxtaposition of sands in the central part of fault F1 (Fig. 13a). This permeable interval is delimited laterally, and at its top, by a relatively thin shale interval. For fault F1, we observe juxtaposed limestone-limestone intervals, together with and sand-shale and sand-silt contacts.

Fault F2, around diapir D1, has a juxtaposition diagram similar to F1 with sand units delimited vertically and laterally by impermeable units (Fig. 13b). Distinctive shale-silt and shale-sand juxtapositions are observed at the centre of this fault. Towards the Southern Area, the juxtaposition diagram for fault F5 shows an upper sand body laterally delimited by silt to the west (Fig. 13c).

The complex geometries of faults located adjacent to diapir D2 are illustrated by the juxtaposition diagram for fault F7 (Figs. 13d). Fault F7 shows a sand-silt juxtaposition in its upper tip towards the west (Fig. 13d). This fault was reactivated towards the east, where juxtaposed sand bodies are not delimited laterally by impermeable units. The lowermost sand interval is delimited by a sand-silt contact to the west and by a shale-silt juxtaposition to the east (Fig. 13d).

Fault F9, adjacent to diapir D1 displays complex juxtaposition of strata (Fig. 13e). The diagram for fault F9 shows a silt-silt juxtaposition at the NW and SE fault terminations, isolating the sand body. Shale-sand and shale-silt contacts are also observed (Fig. 13e). No impermeable (lateral) juxtapositions are observed for faults located adjacent to diapir D3 (Figs. 13f). Fault F11 shows a sand-sand contact delimited vertically by a silt-silt juxtaposition increasing in thickness towards diapir D3. Shale-shale, shale-sand and shale-silt contacts are observed under the sand interval (Fig. 13f).

8. Stress analyses

The existence of only one earthquake focal mechanism in the Espírito Santo Basin, close to the Victoria-Trindade High, the limited seismological coverage in the study area, and the low number of stress measurements for SE Brazil's offshore basins, hinder the determination of a regional stress tensor

for the Espírito Santo Basin (Lima et al., 1997). Furthermore, post-salt deformation is considered to be gravitationally driven, and independent of any basement tectonics (Demercian et al., 1993).

The faulting styles and tectono-stratigraphic evolution of the Espírito Santo Basin point towards an extensional regime in the study area (Chang et al., 1992). Stress inversions for a set of 215 faults in the study area confirm Chang et al. (1992) interpretation by computing a sub-vertical σ_1 plunging -57.89º along an N237.63º azimuth (Table 2). A sub-horizontal σ_3 plunging 17.34º along an N177.46º azimuth was also estimated. Considering that halokinesis resulted, in the study area, in the development of faults with more than two preferential strike directions, we used the results from stress inversions for the faults located in the Salt Ridge to perform slip tendency and leakage factor analyses for the remaining faults F1 to F12. Faults over the Salt Ridge show a more uniform strike and dip distributions when compared to F1 to F12 (Fig. 10). Stress inversions in the Salt Ridge indicate a sub-vertical σ_1 plunging -52.7º along an N187.1º azimuth and a sub-horizontal σ_3 plunging 33º along an N218.6º azimuth (Table 2).

Slip tendency values based on the stress tensor for the Salt Ridge vary from 0.03 to 0.82, showing an average of 0.53 (Fig. 14). The largest slip tendency values, varying from 0.50 to 0.82, are recorded for NW-striking faults, whereas slip tendency ranges from 0 to 0.46 for NE-striking faults (Fig. 14). A similar slip tendency is observed close to D1, with values varying from 0.3 to 0.8 for NW-striking faults and values from 0.0 to 0.3 for faults striking to NE. For the faults in D2, slip tendency ranges from 0.06 to 0.50, with an average slip tendency of 0.34. Most of the faults located around D3 have slip tendency values ranging from 0.02 to 0.25, with NW-striking faults showing the largest slip tendency, from 0.4 to 0.75.

Normalised leakage factors were also estimated considering a fluid pressure of 9 MPa, based on vertical stress measurements (see Zoback, 2010) (Fig. 15). Leakage factor varies from 0.27 to 0.85, indicating a medium to high capacity of faults to leak fluid. Most faults have leakage factors ranging from 0.32 to 0.54, whereas the largest leakage factors, ranging from 0.65 to 0.85, occur in faults in the southern part of the study area (faults F4 and F5) and radial to D3 (Faults F10 and F11). Faults F8 and F7, show distinct leakage factors to the rest of the faults adjacent to D1 and D2 (Fig. 15). Importantly, leakage factors are greater for NW-trending faults than for their NE-striking counterparts (Fig. 15).

9. Discussion

9.1. Structural evolution of the salt structures and timing of faulting

A 3D representation of the interpreted faults in the Espírito Santo Basin is shown in Fig. 16. In order to constrain the timing of faulting, we used horizon H_6 as a time marker. Two main episodes of faulting, pre-Mid-Eocene and post-Mid-Eocene, are defined based on the interpreted stratigraphic relationships between Cretaceous and Paleogene strata, and Throw-depth (T-z) plots for the representative faults F1 to F12.

An important observation on seismic data is the absence of thickness variations on the hanging-wall and footwall blocks of F1 to F12, suggesting that faulting was initiated in the study area after the deposition of Unit 1 (Albian – Middle Eocene, Figs. 4 and 6 to 8). At a regional scale, the first halokinetic movements in the Espírito Santo Basin took place during the Aptian – Albian, resulting from the combination of differential sediment loading, gravity spreading and downslope thin-skinned gravitational gliding above Aptian evaporites (Demercian et al., 1993; Fiduk et al., 2004). Considering the geometry of the interpreted seismic sections (Figs. 4 and 6 to 8), we agree that halokinesis spanning the Aptian to Albian time period deformed post-salt overburden units in the Espírito Santo Basin. However, this deformation was not continuous, and discrete episodes of faulting occurred before the Mid-Eocene as identified in this study. Such an observation agrees with the discrete (and localised) salt deformation that took place in the South Atlantic continental margins during the Albian, Campanian, Paleogene and Neogene (Cobbold et al., 2001; Fiduk and Rowan, 2012; Quirk et al., 2012; Strozyk et al., 2017).

The interpreted seismic cube reveals faults propagating on the crest of salt structures (Figs. 4 and 6 to 8). Faults offsetting salt structures (horizon H_1) include F1, F2, F9 and F11, located at the crests of the Salt Ridge and diapirs D1 and D3 (Figs. 6 and 8). Throw-depth (T-z) data for these faults indicate that a first episode of reactivation occurred in the Albian, as recorded by the throw minima around horizon H_2 (Fig. 12). Away from salt diapirs, seismic reflections seem to be less deformed towards the southern part of the study area (Fig. 6). The relative absence of the salt towards the south, and the occurrence of faults with a throw minima at horizon H_2 (e.g. fault F4), confirm that extension took place during the Albian – Early Eocene.

In faults F10 and F11, the throw minima at horizon H_3 suggest a second reactivation episode close to diapir D3 (Fig. 12). Halokinesis is also apparent for the Salt Ridge and diapirs D1 and D2, as reflected by the displacement minima close to horizon H_5 (sub-unit 1e). We interpret this episode of salt movement as the last halokinetic event recorded on the Salt Ridge, as this structure is now buried by a non-deformed post-salt overburden (Units 2 and 3). Cessation of salt growth resulted in local dissolution of the crest of

527 the Salt Ridge, as shown by the lenticular shape of this salt body on the seismic sections (Fig. 6). The
528 removal of salt occurred preferentially on the crest of salt structures where the salt rises faster, and
529 continued towards the diapir flanks (Ge and Jackson, 1998; Seni and Jackson, 1984).

530 Despite salt dissolution and the pressure exerted by overburden units on the Salt Ridge, no evidence
531 of collapse as in Frumkin et al., (2011), Ge and Jackson, (1998) or Mattos et al., (2016), is observed in
532 the 3D seismic volume for this same structure. This finding contrasts with observations for the eastern
533 part of this seismic volume, where salt withdrawal and collapse play a major role in fault evolution (Alves
534 et al., 2009; Ze and Alves, 2016). Throw-depth (T-z) data for the 12 representative faults, show that
535 displacement decreases towards the Mid-Eocene horizon H_6 (Fig. 12). However, throw for these faults is
536 always greater than zero, as it does not represent the cessation of vertical propagation, hence confirming
537 the removal of part of the Mesozoic strata in the study area(Fig. 12).

538 Our interpretation shows that the bulk of halokinetic movements occurred during the Middle Eocene
539 – Early Miocene, as reflected by the local growth of diapirs D1, D2 and D3. The thinning and folding of
540 Units 1 and 2 on the flanks of salt diapirs reflect post-depositional halokinesis (Figs. 4 and 6 to 8).
541 However, this halokinetic episode had little influence on fault reactivation. No faults were found on the
542 crest of the salt structures, and only a few faults were reactivated after the Mid-Eocene in the western part
543 of the study area. Hence, reactivated faults crossing horizon H_6 include F3, adjacent to D1, and F7
544 adjacent to D3. Throw profiles for these two faults are similar, evidencing a decrease in the throw values
545 for Units 2 and 3 towards their upper tips (Fig. 12).

546 *9.2. Mechanisms of fault linkage and reactivation*

547 Displacement profiles in sections 6.1 and 6.2 provide insights into the mode of propagation and
548 linkage of faults in the western part of the Espírito Santo Basin. Fault geometry and its relationship to
549 adjacent strata are also taken into account when proposing the evolutionary model in this work. For the
550 majority of representative faults, throw-depth (T-z) data show a throw maxima close to horizon H_5 (Fig.
551 12). These faults developed radially to diapirs D2 and D3 (Fig. 11), and in map view radiate out from the
552 diapirs in the direction of other salt structures, where the faults overlap (Fig. 9). Faults developed radially
553 to D1, and the crestal faults in the Salt Ridge seem to be more segmented than those around D2 and D3
554 (Fig. 11). Extension causing the uplift of the Salt Ridge was likely involved in the linkage of the
555 individual fault segments, whereas the successive halokinetic movements of D3 were likely responsible

556 for lateral and vertical propagation of faults that are radial to this structure. Growth in diapirs D1 and D2
557 are also responsible for the lateral segmentation of faults adjacent to these structures.

558 Multiple displacement minima for the faults radial to diapirs (e.g. F3, F7, F10 and F11) indicate that
559 these faults consist of multiple vertically overlapping segments (Fig. 12). For the majority of the
560 representative faults, throw minima occur in sub-unit 1a. The throw-depth profiles indicate larger throw
561 for faults in the western portion of the study area than for the crestal faults found in the eastern part (e.g.
562 Baudon and Cartwright, 2008a). As displacements are larger in the western part of the study area,
563 characteristic throw minima are also observed. The occurrence of successive throw minima on the T-z
564 plots suggests dip-linkage reactivation (Baudon and Cartwright, 2008a; Mansfield and Cartwright, 1996;
565 Omosanya et al., 2015). Dip-linkage reactivation is less common for the faults generated in the eastern
566 part of the study area, as these were chiefly reactivated by upward propagation (Baudon and Cartwright,
567 2008a). Towards the west, dip-linkage seems to be the preferential reactivation mode, with upwards
568 propagation being relatively moderate.

569 Possible explanations for the different modes of reactivation found in the study area include: a)
570 distinct relationships between fault strike and local stress states, and b) radial faults were formed after salt
571 diapir growth, whereas crestal faults propagated in association with regional extension. The orientation of
572 the principal stresses estimated by inverting the faults on the Salt Ridge is NE-SW (Table 2), agrees with
573 the NNE-trending extension direction suggested by Chang et al. (1992) for the SE Brazil. Wherever the
574 orientation of the principal stresses and the strike direction of faults is coincident, there is a greater
575 tendency for faults to reactivate vertically along their length (Baudon and Cartwright, 2008a; Ze and
576 Alves, 2016). The predominant strike direction for the faults in the western part of the Espírito Santo
577 Basin is NW-SE. However, important groups of NE-SW and E-W faults are also found in the study area.
578 In general, the representative faults striking to NNE-SSW display a variable number of throw minima on
579 their throw profiles, whereas NW-SE and E-W striking faults show two negative displacements on their
580 profiles (Fig. 12). Opposing strike and principal stress orientations can, as a result, control the preferential
581 fault reactivation mode, favouring the nucleation of segments with similar dip and strikes.

582 Faults F3 and F7 are the only representative faults that, after a negative break on the throw gradient
583 at the Mid-Eocene horizon H_6, propagated vertically into Units 2 and 3. Faults F3 and F7 strike in
584 opposite directions, NW-SE and NE-SW, respectively. While T-z data for fault F3 indicates a gradual
585 reduction in throw above horizon H_6, fault F7 shows at least six throw minima along its throw profile

(Fig. 12). The T-z for these two faults are an exception to the general pattern of fault growth and evolution observed to the faults in the study area. This indicates that not only regional stress orientations should be considered when assessing fault reactivation, but other local factors, including the presence of overlapping faults (Childs et al., 1995; Kelly et al., 1999) and fault size (Peacock and Sanderson, 1996, 1991), should also be taken into account.

9.3. Implications for petroleum systems in the Espírito Santo Basin

A dense and connected fault network can either constitute a preferential conduit to fluids (Cox et al., 2001; Gartrell et al., 2004) or form barriers to fluid flow as result of shear processes or post-deformation cementation (Gartrell et al., 2003; Sibson, 1996). Crestal and radial faults in the study area comprise corridors connecting distinct salt structures that discretely evolved through time in the Espírito Santo Basin (Fig. 16). The juxtaposition (Allan) diagrams for the study area indicate that faults located radially to D2 and D3, and those located to the south, comprise thicker juxtaposed sands when compared to faults formed close to D1 and the Salt Ridge (Fig. 13). Such an observation is complemented by the presence of bright spots on seismic data. The largest and most continuous bright spots were found in sub-unit 1e adjacently to faults developed radially to diapirs D2 and D3 (Figs. 7 and 8). Faults F9 and F10 offset a bright-spot, meaning these faults can either constitute a possible pathway for fluids or form local seals (Fig. 8). Slip tendency and leakage factor values indicate that F9 could potentially form a competent seal, whereas fault F10 would facilitate fluid flow (Figs. 13 and 14). Bright-spots were also identified at Unit 2, above the faults radial to D3, whereas in the Salt Ridge bright reflections predominate above faults offsetting sub-units 2b and 2c (Fig. 6).

Fault zone complexity limits the analysis of fault-seal behaviour and associated fluid flow paths based solely on seismic data. In fact, important parameters such as the amount and distribution of smeared shales across a fault (Manzocchi et al., 2010), can be overlooked when borehole data are not available (e.g., Caine et al., 1996; Fisher and Knipe, 2001; Koledoye et al., 2003). Apart from variable lithologies and throws, other controls on the transmissibility of fluid in fault zones include their 3D geometry, the conditions that led to their formation, the local stress state(s), the arrangement of structures within a fault zone, interactions between fluids and the host rock, and how all these factors vary in space and time (Caine et al., 1996).

615 Leakage factor calculations indicate two different trends for the interpreted faults. The great majority
616 of faults shows a leakage factor ranging from 0.3 to 0.5, suggesting that sealing units were juxtaposed
617 during faulting and implying a smaller leakage potential (Fig. 15). Juxtaposition diagrams reveal that for
618 F2 and F5, sealing units isolate the intervals units and potentially hinder fluid migration (Fig. 13). A
619 second leakage factor trend for the study area ranges from 0.6 to 0.8, showing a greater potential to leak
620 fluids. The parts of the fault where leakage seems to be occurring coincides with the parts of the fault that
621 are most likely to slip. This constitutes evidence that fault slip is the main mechanism responsible for
622 fluid leakage in a direction parallel to faults (Barton et al., 1995; Wiprut and Zoback, 2000). Largest
623 leakage factors for faults adjacent to D1, D2 and D3 coincide with the fault terminations close to these
624 same salt diapirs. Faults with large leakage factors include the NW-striking crestal faults, faults adjacent
625 to diapirs D2 and D3, and a number of faults in the southern part of the study area (Fig. 15).
626 Based on our results, we propose that corridors of faults developed around the interpreted salt
627 structures form a preferential pathway for fluids in the study area. Hence, fluid tends to migrate through
628 the faults towards the shallowest diapirs and stratigraphic units (Fig. 16). The preferential fluid pathway
629 in this fault corridor is from south to north-northwest, where the densest accumulation of bright
630 reflections is observed and cross-cut faults developed radially to D3, or above the Salt Ridge (Fig. 16). In
631 such a setting, the combined use of stress analyses and juxtaposition diagrams show that reservoir units
632 within the Espírito Santo Basin are connected through corridors of faults that were developed during the
633 Cretaceous and the Paleogene in association with successive reactivation episodes.
634

635 **10. Conclusions**

636 This work aimed at understanding if there was a main reactivation style for faults on the continental
637 slope of the Espírito Santo Basin, and how this reactivation controls fluid flow. The main conclusions of
638 this work are summarised as follows:

639 a) Faults in the study area can be divided into five distinct families according to their location relative to
640 the salt structures. Radial faults occur adjacent to three salt diapirs (D1, D2 and D3), and crestal faults
641 were developed over a NW-trending Salt Ridge. The fifth family of faults occurs in the southern half
642 of the study area, a region that was less affected by halokinesis. The largest faults are NW-trending,
643 whereas the predominant orientations of the smaller faults are NE-SW and E-W.

644 b) Salt structures evolved in two distinct phases; the first before the Middle Eocene, associated with
645 moderate halokinetic deformation and faulting, and the second after the Middle Eocene recording
646 intense halokinesis. Our observations indicate that the growth of the Salt Ridge was the first to cease
647 in the study area. The growth of diapirs D1 to D3 resulted in the formation of radial faults around
648 them.
649 c) We found that preferential NE-SW reactivation took place based on the paleostress inversion
650 performed in this work. The inversion results show that the study area was subjected to NNE-SSW
651 extension. Dip-linked reactivation seems to be the preferential reactivation mode for the faults formed
652 in the western part of the study area, contrasting with the eastern part where reactivation by vertical
653 (upward) propagation predominates. Strata younger than the Middle Eocene were barely faulted,
654 except for faults F3 and F7.
655 d) Slip tendency and leakage factor analysis, combined with juxtaposition diagrams, indicate that the
656 areas most prone to leak fluids occur adjacently to diapirs D1, D2 and D3.
657 e) Our model proposes that faults are mainly extensional and comprise structural corridors that connect
658 different salt structures. These corridors form a preferential path for fluid flow from south to north-
659 northwest. In such a setting, diapir D3 is the shallowest salt structure in the study area onto which
660 fluid migrates from deeper salt structures to accumulate on its flanks.
661

662 **Acknowledgements**

663 The authors would like to acknowledge the permission conceded by CGG for the use of the seismic
664 data presented in this paper. The first author would like to acknowledge CAPES (Coordenação de
665 Aperfeiçoamento de Pessoal de Nível Superior – Brazil) for the PhD scholarship under process no.
666 0877/14-0. Schlumberger (providers of Petrel®), Midland Valley (Move®) and the Southwest Research
667 Institute (3D Stress®) are acknowledged for the provision of the academic licences to Cardiff University
668 3D Seismic Lab. We thank editor Zheng-Xiang Li, Peter Kukla and an anonymous reviewer for their
669 constructive comments.

670 **References**

671 Ainsworth, R.B., 2006. Sequence stratigraphic-based analysis of reservoir connectivity: influence of
672 sealing faults - a case study from a marginal marine depositional setting. Pet. Geosci.
673 doi:10.1144/1354-079305-661

674 Allan, U.S., 1989. Model for hydrocarbon migration and entrapment within faulted structures. Am.
675 Assoc. Pet. Geol. Bull. 73, 803–811.

676 Alves, T.M., 2012. Scale-relationships and geometry of normal faults reactivated during gravitational
677 gliding of Albian rafts (Espírito Santo Basin, SE Brazil). Earth Planet. Sci. Lett. 331, 80–96.

678 Alves, T.M., Cartwright, J., Davies, R.J., 2009. Faulting of salt-withdrawal basins during early
679 halokinesis: effects on the Paleogene Rio Doce Canyon system (Espírito Santo Basin, Brazil). Am.
680 Assoc. Pet. Geol. Bull. 93, 617–652.

681 Bailey, W.R., Manzocchi, T., Walsh, J.J., Keogh, K., Hodgetts, D., Rippon, J., Nell, P.A.R., Flint, S.,
682 Strand, J.A., 2002. The effect of faults on the 3D connectivity of reservoir bodies: a case study from
683 the East Pennine Coalfield, UK. Pet. Geosci. 8, 263–277. doi:10.1144/petgeo.8.3.263

684 Barker, P.F., Buffler, R.T., Gambôa, L.A., 1983. A seismic reflection study of the Rio Grande Rise.
685 Initial Reports Deep Sea Drill. Proj. 72, 499–517.

686 Barnett, J.A.M., Mortimer, J., Rippon, J.H., Walsh, J.J., Watterson, J., 1987. Displacement geometry in
687 the volume containing a single normal fault. Am. Assoc. Pet. Geol. Bull. 71, 925–937.

688 Barton, C.A., Zoback, M.D., Moos, D., 1995. Fluid flow along potentially active faults in crystalline rock.
689 Geology 23, 683–686.

690 Baudon, C., Cartwright, J., 2008a. The kinematics of reactivation of normal faults using high resolution
691 throw mapping. J. Struct. Geol. 30, 1072–1084. doi:10.1016/j.jsg.2008.04.008

692 Baudon, C., Cartwright, J. a., 2008b. 3D seismic characterisation of an array of blind normal faults in the
693 Levant Basin, Eastern Mediterranean. J. Struct. Geol. 30, 746–760. doi:10.1016/j.jsg.2007.12.008

694 Brown, A.R., 2011. Interpretation of three-dimensional seismic data. American Association of Petroleum
695 Geologists and the Society of Exploration Geophysicists.

696 Bruhn, C.H.L., Gomes, J.A.T., Del Lucchese Jr, C., Johann, P.R.S., 2003. Campos basin: reservoir
697 characterization and management-Historical overview and future challenges, in: Offshore
698 Technology Conference. Offshore Technology Conference.

699 Bruhn, C.H.L., Walker, R.G., 1997. Internal architecture and sedimentary evolution of coarse-grained,
700 turbidite channel-levee complexes, Early Eocene Regencia Canyon, Espirito Santo Basin, Brazil.
701 Sedimentology 44, 17–46.

702 Brun, J.-P., Fort, X., 2011. Salt tectonics at passive margins: Geology versus models. Mar. Pet. Geol. 28,
703 1123–1145. doi:10.1016/j.marpetgeo.2011.03.004

704 Caine, J.S., Evans, J.P., Forster, C.B., 1996. Fault zone architechture and permeability structure. Geology
705 24, 1025–1028. doi:10.1130/0091-7613(1996)024<1025

706 Cainelli, C., Mohriak, W.U., 1999. Some remarks on the evolution of sedimentary basins along the
707 Eastern Brazilian continental margin. Episodes-Newsmagazine Int. Union Geol. Sci. 22, 206–216.

708 Cainelli, C., Mohriak, W.U., 1998. Geology of Atlantic eastern Brazilian basins, in: Brazilian Geology

709 Part. p. 1998.

710 Carruthers, D., Cartwright, J., Jackson, M.P. a., Schutjens, P., 2013. Origin and timing of layer-bound
711 radial faulting around North Sea salt stocks: New insights into the evolving stress state around
712 rising diapirs. Mar. Pet. Geol. 48, 130–148. doi:10.1016/j.marpetgeo.2013.08.001

713 Cartwright, J.A., Mansfield, C.S., 1998. Lateral displacement variation and lateral tip geometry of normal
714 faults in the Canyonlands National Park, Utah. J. Struct. Geol. doi:10.1016/S0191-8141(97)00079-5

715 Chand, S., Mienert, J., Andreassen, K., Knies, J., Plassen, L., Fotland, B., 2008. Gas hydrate stability
716 zone modelling in areas of salt tectonics and pockmarks of the Barents Sea suggests an active
717 hydrocarbon venting system. Mar. Pet. Geol. 25, 625–636. doi:10.1016/j.marpetgeo.2007.10.006

718 Chang, H.K., Kowsmann, R.O., Figueiredo, A.M.F., Bender, A., 1992. Tectonics and stratigraphy of the
719 East Brazil Rift system: an overview. Tectonophysics 213, 97–138.

720 Childs, C., Walsh, J.J., Watterson, J., 1997. Complexity in fault zone structure and implications for fault
721 seal prediction. Nor. Pet. Soc. Spec. Publ. 7, 61–72. doi:10.1016/S0928-8937(97)80007-0

722 Childs, C., Watterson, J., Walsh, J.J., 1995. Fault overlap zones within developing normal fault systems.
723 J. Geol. Soc. London. doi:10.1144/gsjgs.152.3.0535

724 Cobbold, P.R., Meisling, K.E., Mount, V.S., 2001. Reactivation of an obliquely rifted margin, Campos
725 and Santos basins, southeastern Brazil. Am. Assoc. Pet. Geol. Bull. 85, 1925–1944.

726 Cowie, P.A., Scholz, C.H., 1992. Physical Explanation for the Displacement Length Relationship of
727 Faults Using a Post-Yield Fracture-Mechanics Model. J. Struct. Geol. 14, 1133–1148.

728 Cox, S.F., Knackstedt, M.A., Braun, J., 2001. Principles of structural control on permeability and fluid
729 flow in hydrothermal systems. Rev. Econ. Geol. 14, 1–24.

730 Demercian, S., Szatmari, P., Cobbold, P.R., 1993. Style and pattern of salt diapirs due to thin-skinned
731 gravitational gliding, Campos and Santos basins, offshore Brazil. Tectonophysics 228, 393–433.
732 doi:10.1016/0040-1951(93)90351-J

733 Diegel, F.A., Karlo, J.F., Schuster, D.C., Shoup, R.C., Tauvers, P.R., 1995. Cenozoic structural evolution
734 and tectono-stratigraphic framework of the northern Gulf Coast continental margin.

735 Duval, B., Cramez, C., Jackson, M.P. a., 1992. Raft tectonics in the Kwanza Basin, Angola. Mar. Pet.
736 Geol. 9, 389–404. doi:10.1016/0264-8172(92)90050-O

737 Estrella, G., Mello, M.R., Gaglianone, P.C., Azevedo, R.L.M., Tsubone, K., Rossetti, E., Concha, J.,
738 Bruning, I., 1984. The Espirito Santo Basin (Brazil) source rock characterization and petroleum
739 habitat.

740 Faulkner, D.R., Jackson, C.A.L., Lunn, R.J., Schlische, R.W., Shipton, Z.K., Wibberley, C.A.J.,
741 Withjack, M.O., 2010. A review of recent developments concerning the structure, mechanics and
742 fluid flow properties of fault zones. J. Struct. Geol. doi:10.1016/j.jsg.2010.06.009

743 Ferrill, D.A., Morris, A.P., McGinnis, R.N., 2009. Crossing conjugate normal faults in field exposures

744 and seismic data. Am. Assoc. Pet. Geol. Bull. 93, 1471–1488.

745 Fiduk, J.C., Brush, E.R., Anderson, L.E., Gibbs, P.B., Rowan, M.G., 2004. Salt deformation, magmatism,
746 and hydrocarbon prospectivity in the Espirito Santo Basin, offshore Brazil, in: Salt-Sediment
747 Interactions and Hydrocarbon Prospectivity: Concepts, Applications, and Case Studies for the 21st
748 Century: Gulf Coast Section SEPM 24th Annual Conference. p. 370.

749 Fiduk, J.C., Rowan, M.G., 2012. Analysis of folding and deformation within layered evaporites in Blocks
750 BM-S-8 &-9, Santos Basin, Brazil. Geol. Soc. London, Spec. Publ. 363, 471–487.

751 Figueiredo, A.M.F., Mohriak, W.U., 1984. A tectonica salifera e as acumulacoes de Petroleo da Bacia de
752 Campos, in: Proceedings of the 33rd Brazilian Geological Congress, Sociedada Brasileira de
753 Geologia, Rio de Janeiro. pp. 1380–1394.

754 Fisher, Q.J., Knipe, R.J., 2001. The permeability of faults within siliciclastic petroleum reservoirs of the
755 North Sea and Norwegian Continental Shelf. Mar. Pet. Geol. 18, 1063–1081.

756 França, R.L., Del Rey, A.C., Tagliari, C.V., Brandão, J.R., Fontanelli, P. de R., 2007. Bacia do Espírito
757 Santo. Bol. Geociencias da PETROBRAS 15, 501–509.

758 Frumkin, A., Ezersky, M., Al-Zoubi, A., Akkawi, E., Abueladas, A.-R., 2011. The Dead Sea sinkhole
759 hazard: Geophysical assessment of salt dissolution and collapse. Geomorphology 134, 102–117.

760 Gamboa, D.A., 2011. An integrated seismic-scale analysis of reservoir compartmentalisation on
761 continental margins: the Espirito Santo Basin, SE Brazil.

762 Gamboa, D., Alves, T., Cartwright, J., Terrinha, P., 2010. MTD distribution on a “passive” continental
763 margin: The Espírito Santo Basin (SE Brazil) during the Palaeogene. Mar. Pet. Geol. 27, 1311–
764 1324. doi:10.1016/j.marpetgeo.2010.05.008

765 Gamboa, D., Alves, T.M., 2015. Spatial and dimensional relationships of submarine slope architectural
766 elements: A seismic-scale analysis from the Espírito Santo Basin (SE Brazil). Mar. Pet. Geol. 64,
767 43–57.

768 Gamboa, D., Alves, T.M., Cartwright, J., 2012. A submarine channel confluence classification for
769 topographically confined slopes. Mar. Pet. Geol. 35, 176–189.
770 doi:10.1016/j.marpetgeo.2012.02.011

771 Gartrell, A., Zhang, Y., Lisk, M., Dewhurst, D., 2004. Fault intersections as critical hydrocarbon leakage
772 zones: integrated field study and numerical modelling of an example from the Timor Sea, Australia.
773 Mar. Pet. Geol. 21, 1165–1179. doi:10.1016/j.marpetgeo.2004.08.001

774 Gartrell, A., Zhang, Y., Lisk, M., Dewhurst, D., 2003. Enhanced hydrocarbon leakage at fault
775 intersections: an example from the Timor Sea, Northwest Shelf, Australia. J. Geochemical Explor.
776 78, 361–365.

777 Ge, H., Jackson, M.P.A., 1998. Physical modeling of structures formed by salt withdrawal: Implications
778 for deformation caused by salt dissolution. Am. Assoc. Pet. Geol. Bull. 82, 228–250.

779 Guardado, L.R., Spadini, A.R., Brandão, J.S.L., Mello, M.R., 2000. Petroleum System of the Campos

780 Basin, Brazil. AAPG Mem. 73.

781 Guerra, M.C.M., Underhill, J.R., 2012. Role of halokinesis in controlling structural styles and sediment
782 dispersal in the Santos Basin, offshore Brazil. Geol. Soc. London, Spec. Publ. 363, 175–206.

783 Henriksen, E., Ryseth, A.E., Larssen, G.B., Heide, T., Ronning, K., Sollid, K., Stoupakova, A. V., 2011.
784 Tectonostratigraphy of the greater Barents Sea: implications for petroleum systems. Geol. Soc.
785 London, Mem. doi:10.1144/M35.10

786 Hudec, M.R., Jackson, M.P.A., 2002. Structural segmentation, inversion, and salt tectonics on a passive
787 margin: Evolution of the Inner Kwanza Basin, Angola. Geol. Soc. Am. Bull. 114, 1222–1244.

788 Hudec, M.R., Jackson, M.P. a., 2007. Terra infirma: Understanding salt tectonics. Earth-Science Rev. 82,
789 1–28. doi:10.1016/j.earscirev.2007.01.001

790 Jackson, M.P.A., Vendeville, B.C., Schultz-Ela, D.D., 1994. Structural Dynamics of Salt Systems. Annu.
791 Rev. Earth Planet. Sci. 22, 93–117. doi:10.1146/annurev.ea.22.050194.000521

792 Jolley, S.J., Barr, D., Walsh, J.J., Knipe, R.J., 2007. Structurally complex reservoirs: an introduction.
793 Geol. Soc. London, Spec. Publ. 292, 1–24.

794 Jolley, S.J., Fisher, Q.J., Ainsworth, R.B., 2010. Reservoir compartmentalization: an introduction. Geol.
795 Soc. London, Spec. Publ. 347, 1–8. doi:10.1144/SP347.1

796 Jones, R.M., Hillis, R.R., 2003. An integrated, quantitative approach to assessing fault-seal risk. Am.
797 Assoc. Pet. Geol. Bull. 87, 507–524.

798 Kane, K.E., Jackson, C. a.-L., Larsen, E., 2010. Normal fault growth and fault-related folding in a salt-
799 influenced rift basin: South Viking Graben, offshore Norway. J. Struct. Geol. 32, 490–506.
800 doi:10.1016/j.jsg.2010.02.005

801 Katz, B.J., Mello, M.R., 2000. Petroleum Systems of South Atlantic Marginal Basins - An Overview.
802 AAPG Mem. 73.

803 Kelly, P.G., Peacock, D.C.P., Sanderson, D.J., McGurk, A.C., 1999. Selective reverse-reactivation of
804 normal faults, and deformation around reverse-reactivated faults in the Mesozoic of the Somerset
805 coast. J. Struct. Geol. 21, 493–509. doi:10.1016/S0191-8141(99)00041-3

806 Knipe, R.J., 1997. Juxtaposition and seal diagrams to help analyze fault seals in hydrocarbon reservoirs.
807 Am. Assoc. Pet. Geol. Bull. 81, 187–195. doi:10.1306/522B42DF-1727-11D7-8645000102C1865D

808 Knipe, R.J., Jones, G., Fisher, Q.J., 1998. Faulting, fault sealing and fluid flow in hydrocarbon reservoirs:
809 an introduction. Geol. Soc. London, Spec. Publ. doi:10.1144/GSL.SP.1998.147.01.01

810 Koledoye, B.A., Aydin, A., May, E., 2003. A new process-based methodology for analysis of shale smear
811 along normal faults in the Niger Delta. Am. Assoc. Pet. Geol. Bull. 87, 445–463.

812 Koyi, H., Talbot, C.J., Tørudbakken, B.O., 1993. Salt diapirs of the southwest Nordkapp Basin: analogue
813 modelling. Tectonophysics 228, 167–187.

814 Lima, C., Nascimento, E., Assumpção, M., 1997. Stress orientations in Brazilian sedimentary basins from

breakout analysis: implications for force models in the South American plate. Geophys. J. Int. 130, 112–124.

Lohr, T., Krawczyk, C.M., Tanner, D.C., Samiee, R., Endres, H., Thierer, P.O., Oncken, O., Trappe, H., Bachmann, R., Kukla, P.A., 2008. Prediction of subseismic faults and fractures: Integration of three-dimensional seismic data, three-dimensional retrodeformation, and well data on an example of deformation around an inverted fault. Am. Assoc. Pet. Geol. Bull. 92, 473–485.

Mansfield, C.S., Cartwright, J.A., 1996. High resolution fault displacement mapping from three-dimensional seismic data: evidence for dip linkage during fault growth. J. Struct. Geol. 18, 249–263. doi:10.1016/S0191-8141(96)80048-4

Manzocchi, T., Childs, C., Walsh, J.J., 2010. Faults and fault properties in hydrocarbon flow models. Geofluids 10, 94–113.

Mattos, N.H., Alves, T.M., Omosanya, K.O., 2016. Crestal fault geometries reveal late halokinesis and collapse of the Samson Dome, Northern Norway: Implications for petroleum systems in the Barents Sea. Tectonophysics.

McFarland, J.M., Morris, A.P., Ferrill, D.A., 2012. Stress inversion using slip tendency. Comput. Geosci. 41, 40–46.

Meisling, K.E., Cobbold, P.R., Mount, V.S., 2001. Segmentation of an obliquely rifted margin, Campos and Santos basins, southeastern Brazil. Am. Assoc. Pet. Geol. Bull. 85, 1903–1924.

Milani, E.J., Brandão, J.A.S.L., Zalán, P. V., Gamboa, L.A.P., 2001. Petróleo na Margem Continental Brasileira: Geologia, exploração, resultados e perspectivas. Brazilian J. Geophys. 18, 351–396.

Mohriak, W.U., 2005. Interpretação geológica e geofísica da Bacia do Espírito Santo e da região de Abrolhos: petrografia, datações radiométricas e visualização sísmica das rochas vulcânicas. Bol. Geoc. Petrobrás 14, 133–142.

Mohriak, W.U., 2003. Bacias sedimentares da margem continental Brasileira. Geol. Tectônica e Recur. Minerais do Bras. 87–165.

Mohriak, W.U., Nemčok, M., Enciso, G., 2008. South Atlantic divergent margin evolution: rift-border uplift and salt tectonics in the basins of SE Brazil. Geol. Soc. London, Spec. Publ. 294, 365–398.

Moraes, M.A.S., Maciel, W.B., Braga, M.S.S., Viana, A.R., 2007. Bottom-current reworked Palaeocene-Eocene deep-water reservoirs of the Campos Basin, Brazil. Geol. Soc. London, Spec. Publ. 276, 81–94.

Morley, C.K., Guerin, G., 1996. Comparison of gravity-driven deformation styles and behavior associated with mobile shales and salt. Tectonics 15, 1154–1170.

Morris, A., Ferrill, D. a, Henderson, D.B., 1996. Slip-tendency analysis and fault reactivation. Geology 24, 275–278. doi:10.1130/0091-7613(1996)024<0275

Muraoka, H., Kamata, H., 1983. Displacement distribution along minor fault traces. J. Struct. Geol. 5, 483–495. doi:10.1016/0191-8141(83)90054-8

851 Nicol, A., Gillespie, P.A., Childs, C., Walsh, J.J., 2002. Relay zones between mesoscopic thrust faults in
852 layered sedimentary sequences. J. Struct. Geol. 24, 709–727.

853 Nicol, A., Watterson, J., Walsh, J.J., Childs, C., 1996. The shapes, major axis orientations and
854 displacement patterns of fault surfaces. J. Struct. Geol. doi:10.1016/S0191-8141(96)80047-2

855 Ojeda, H.A.O., 1982. Structural framework, stratigraphy, and evolution of Brazilian marginal basins. Am.
856 Assoc. Pet. Geol. Bull. 66, 732–749.

857 Omosanya, K.O., Alves, T.M., 2014. Mass-transport deposits controlling fault propagation, reactivation
858 and structural decoupling on continental margins (Espírito Santo Basin, SE Brazil). Tectonophysics
859 628, 158–171. doi:http://dx.doi.org/10.1016/j.tecto.2014.04.045

860 Omosanya, K.O., Alves, T.M., 2013. A 3-dimensional seismic method to assess the provenance of Mass-
861 Transport Deposits (MTDs) on salt-rich continental slopes (Espírito Santo Basin, SE Brazil). Mar.
862 Pet. Geol. 44, 223–239. doi:10.1016/j.marpetgeo.2013.02.006

863 Omosanya, K.O., Johansen, S.E., Harishidayat, D., 2015. Evolution and character of supra-salt faults in
864 the Easternmost Hammerfest Basin, SW Barents Sea. Mar. Pet. Geol.

865 Peacock, D.C.P., Sanderson, D.J., 1996. Effects of propagation rate on displacement variations along
866 faults. J. Struct. Geol. 18, 311–320.

867 Peacock, D.C.P., Sanderson, D.J., 1991. Displacements, segment linkage and relay ramps in normal fault
868 zones. J. Struct. Geol. 13, 721–733. doi:10.1016/0191-8141(91)90033-F

869 Quirk, D.G., Schødt, N., Lassen, B., Ings, S.J., Hsu, D., Hirsch, K.K., Von Nicolai, C., 2012. Salt
870 tectonics on passive margins: examples from Santos, Campos and Kwanza basins. Geol. Soc.
871 London, Spec. Publ. 363, 207–244.

872 Reilly, C., Nicol, A., Walsh, J.J., Kroeger, K.F., 2016. Temporal changes of fault seal and early charge of
873 the Maui Gas-condensate field, Taranaki Basin, New Zealand. Mar. Pet. Geol. 70, 237–250.

874 Rowan, M.G., Jackson, M.P.A., Trudgill, B.D., 1999. Salt-related fault families and fault welds in the
875 northern Gulf of Mexico. Am. Assoc. Pet. Geol. Bull. doi:10.1306/E4FD41E3-1732-11D7-
876 8645000102C1865D

877 Scholz, C.H., Cowie, P.A., 1990. Determination of total strain from faulting using slip measurements.

878 Seni, S.J., Jackson, M.P.A., 1984. Sedimentary Record of Cretaceous and Tertiary Salt Movement, East
879 Texas Basin: Times, Rates, and Volumes of Salt Flow and Their Implications for Nuclear Waste
880 Isolation and Petroleum Exploration. Bureau of Economic Geology, University of Texas of Austin.

881 Sheriff, R.E., Geldart, L.P., 1995. Exploration Seismology, Second Edi. ed. Cambridge University Press,
882 Cambridge. doi:10.1017/CBO9781139168359

883 Sibson, R.H., 1996. Structural permeability of fluid-driven fault-fracture meshes. J. Struct. Geol. 18,
884 1031–1042.

885 Smit, J., Brun, J.-P., Fort, X., Cloetingh, S., Ben-Avraham, Z., 2008. Salt tectonics in pull-apart basins

886 with application to the Dead Sea Basin. Tectonophysics 449, 1–16. doi:10.1016/j.tecto.2007.12.004

887 Stewart, S. a., 2006. Implications of passive salt diapir kinematics for reservoir segmentation by radial
888 and concentric faults. Mar. Pet. Geol. 23, 843–853. doi:10.1016/j.marpetgeo.2006.04.001

889 Strozyk, F., Back, S., Kukla, P.A., 2017. Comparison of the rift and post-rift architecture of conjugated
890 salt and salt-free basins offshore Brazil and Angola/Namibia, South Atlantic. Tectonophysics 716,
891 204-224. doi:10.1016/j.tecto.2016.12.012.

892 Talbot, C., Rönnlund, P., Schmeling, H., 1991. Diapiric spoke patterns. Tectonophysics 188, 187–201.

893 Talbot, C.J., 1993. Spreading of salt structures in the Gulf of Mexico. Tectonophysics 228, 151–166.
894 doi:10.1016/0040-1951(93)90338-K

895 Varela, C.L., Mohriak, W.U., 2013. Halokinetic rotating faults, salt intrusions, and seismic pitfalls in the
896 petroleum exploration of divergent margins. Am. Assoc. Pet. Geol. Bull. doi:10.1306/02261312164

897 Vendeville, B.C., 2002. A new interpretation of Trusheim's classic model of salt-diapir growth.

898 Vendeville, B.C., Jackson, M.P. a., 1992. The rise of diapirs during thin-skinned extension. Mar. Pet.
899 Geol. 9, 331–354. doi:10.1016/0264-8172(92)90047-I

900 Viana, A., Figueiredo, A., Faugres, J.-C., Lima, A., Gonthier, E., Brehme, I., Zaragosi, S., 2003. The São
901 Tomé deep-sea turbidite system (southern Brazil Basin): Cenozoic seismic stratigraphy and
902 sedimentary processes. Am. Assoc. Pet. Geol. Bull. 87, 873–894.

903 Vieira, R.A.B., Mendes, M.P., Vieira, P.E., Costa, L.A.R., Tagliari, C. V, Bacelar, L.A.P., Feijó, F.J.,
904 1994. Bacias do Espírito Santo e Mucuri. Bol. Geosci. da Petrobrás, Rio Janeiro 8, 191–202.

905 Walsh, J.J., Bailey, W.R., Childs, C., Nicol, A., Bonson, C.G., 2003. Formation of segmented normal
906 faults: a 3-D perspective. J. Struct. Geol. 25, 1251–1262.

907 Walsh, J.J., Nicol, A., Childs, C., 2002. An alternative model for the growth of faults. J. Struct. Geol. 24,
908 1669–1675. doi:10.1016/S0191-8141(01)00165-1

909 Walsh, J.J., Watterson, J., 1989. Displacement gradients on fault surfaces. J. Struct. Geol.
910 doi:10.1016/0191-8141(89)90070-9

911 Walsh, J.J., Watterson, J., 1987. Distributions of cumulative displacement and seismic slip on a single
912 normal fault surface. J. Struct. Geol. doi:10.1016/0191-8141(87)90012-5

913 Walsh, J.J., Watterson, J., Heath, A.E., Childs, C., 1998. Representation and scaling of faults in fluid flow
914 models. Pet. Geosci. doi:10.1144/petgeo.4.3.241

915 Wiprut, D., Zoback, M.D., 2000. Fault reactivation and fluid flow along a previously dormant normal
916 fault in the northern North Sea. Geology 28, 595–598.

917 Ze, T., Alves, T.M., 2016. The role of gravitational collapse in controlling the evolution of crestal fault
918 systems (Espírito Santo Basin, SE Brazil). J. Struct. Geol. 92, 79–98.

919 Zoback, M.D., 2010. Reservoir geomechanics. Cambridge University Press.

920

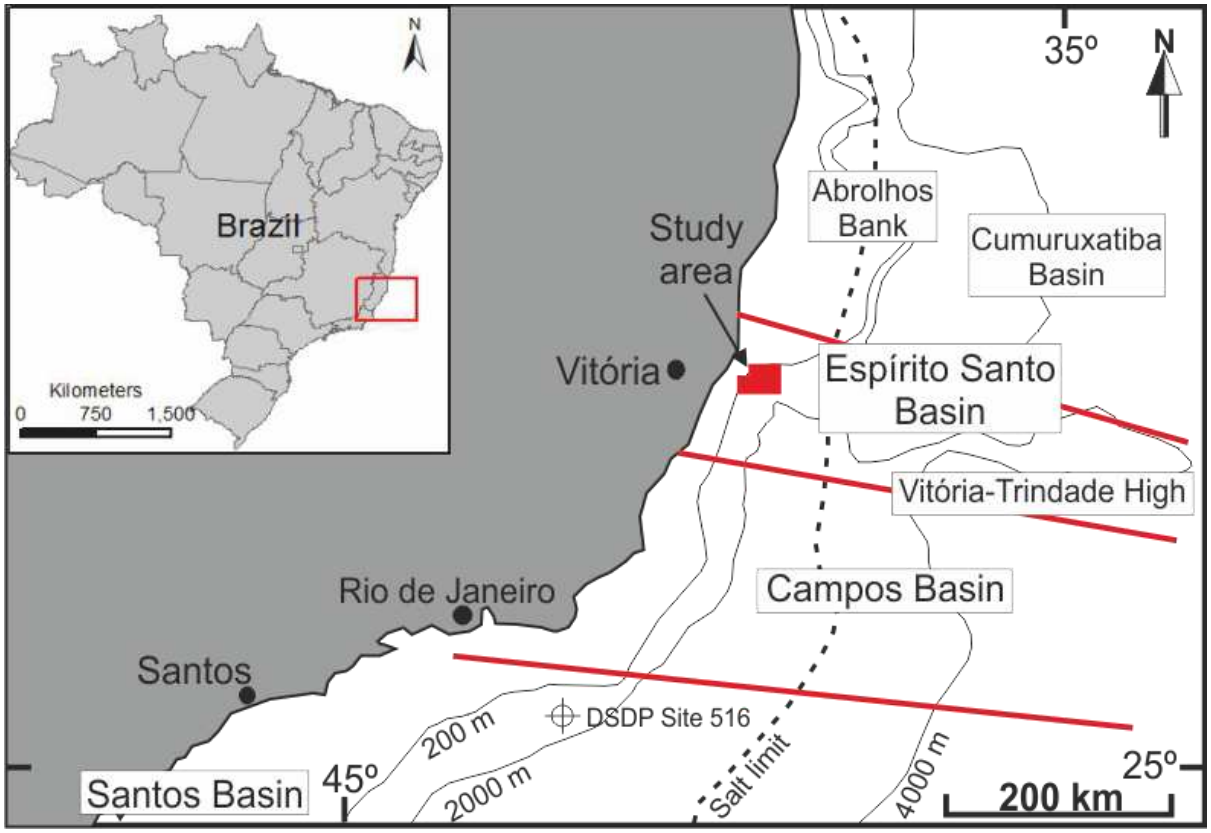

Figure 1: Location map of the Espírito Santo Basin and its main boundaries. The Espírito Santo Basin is limited to the north by the Abrolhos Bank and to the south by the Vitória-Trindade High. The location of the 3D seismic cube is indicated by the red polygon.

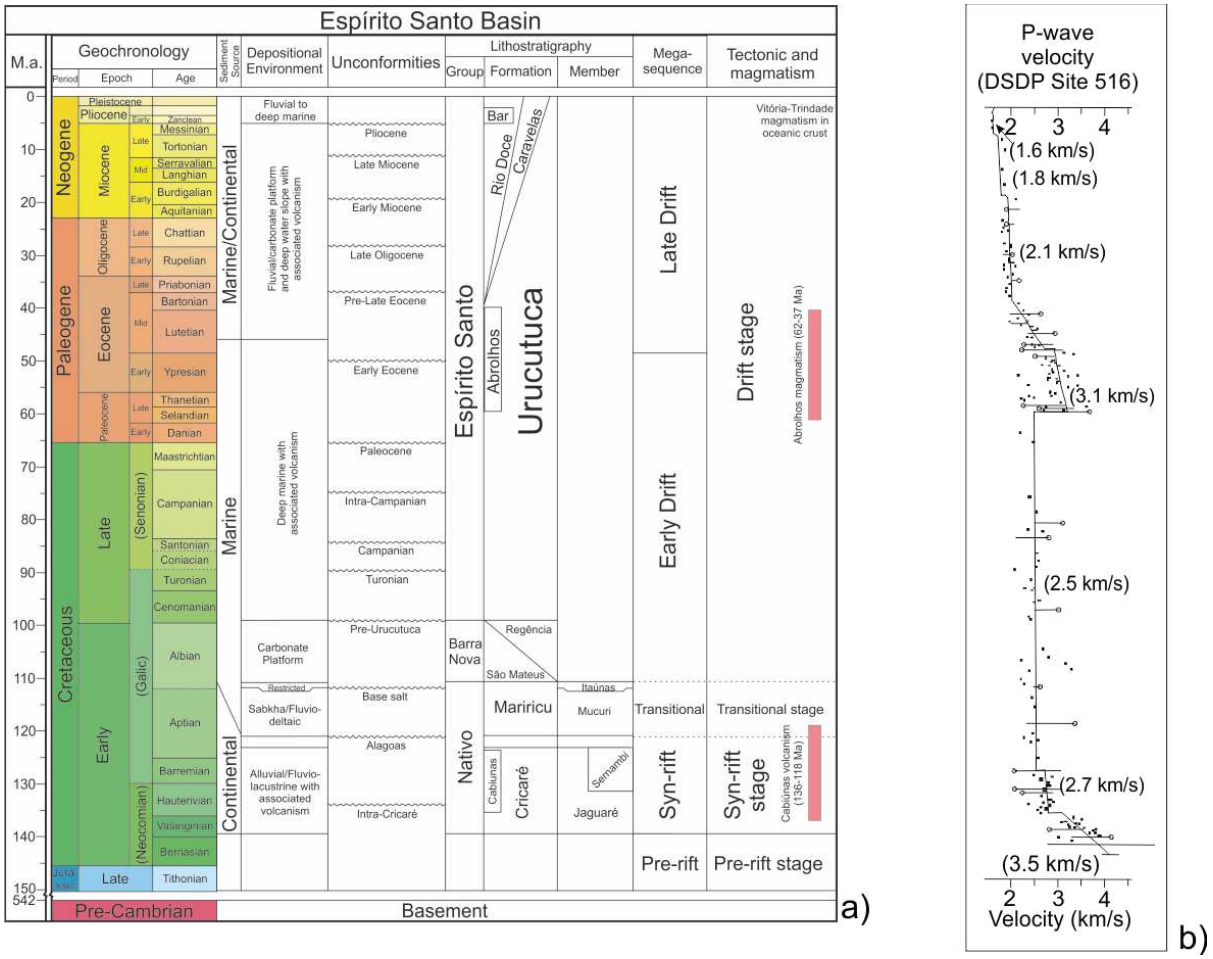

Figure 2: Stratigraphic column of the Espírito Santo Basin highlighting main sediment sources and depositional environments. Four tectonic stages and five depositional megasequences are documented in the basin (Modified from França et al., 2007).Velocity data for well DSDP Site 516 for the Rio Grande Rise compiled from Barker et al. (1983).

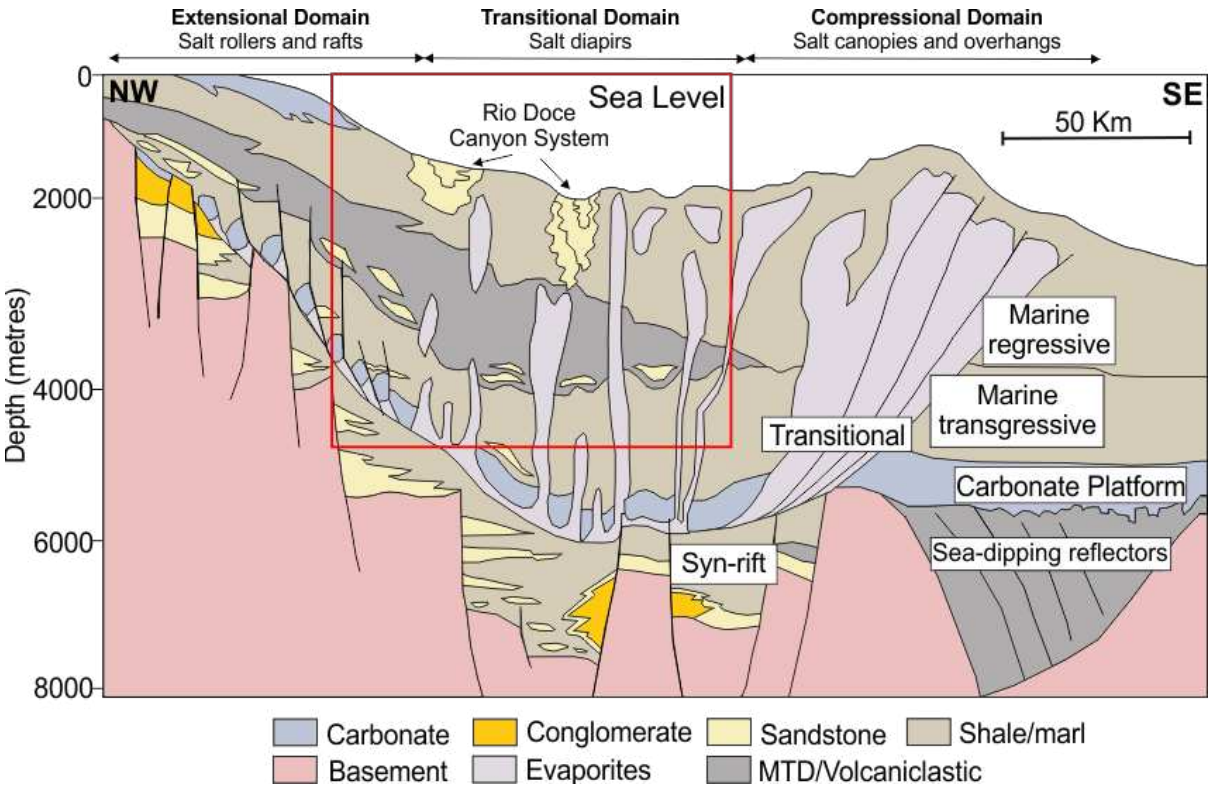

Figure 3: Simplified regional section of the Espírito Santo Basin showing major depositional sequences and salt structures across three structural domains: extensional, transitional and compressional. The approximate location of the study area is shown by the red polygon, within the extensional and transitional domains. Modified from Fiduk et al. (2004) and Gamboa (2011).

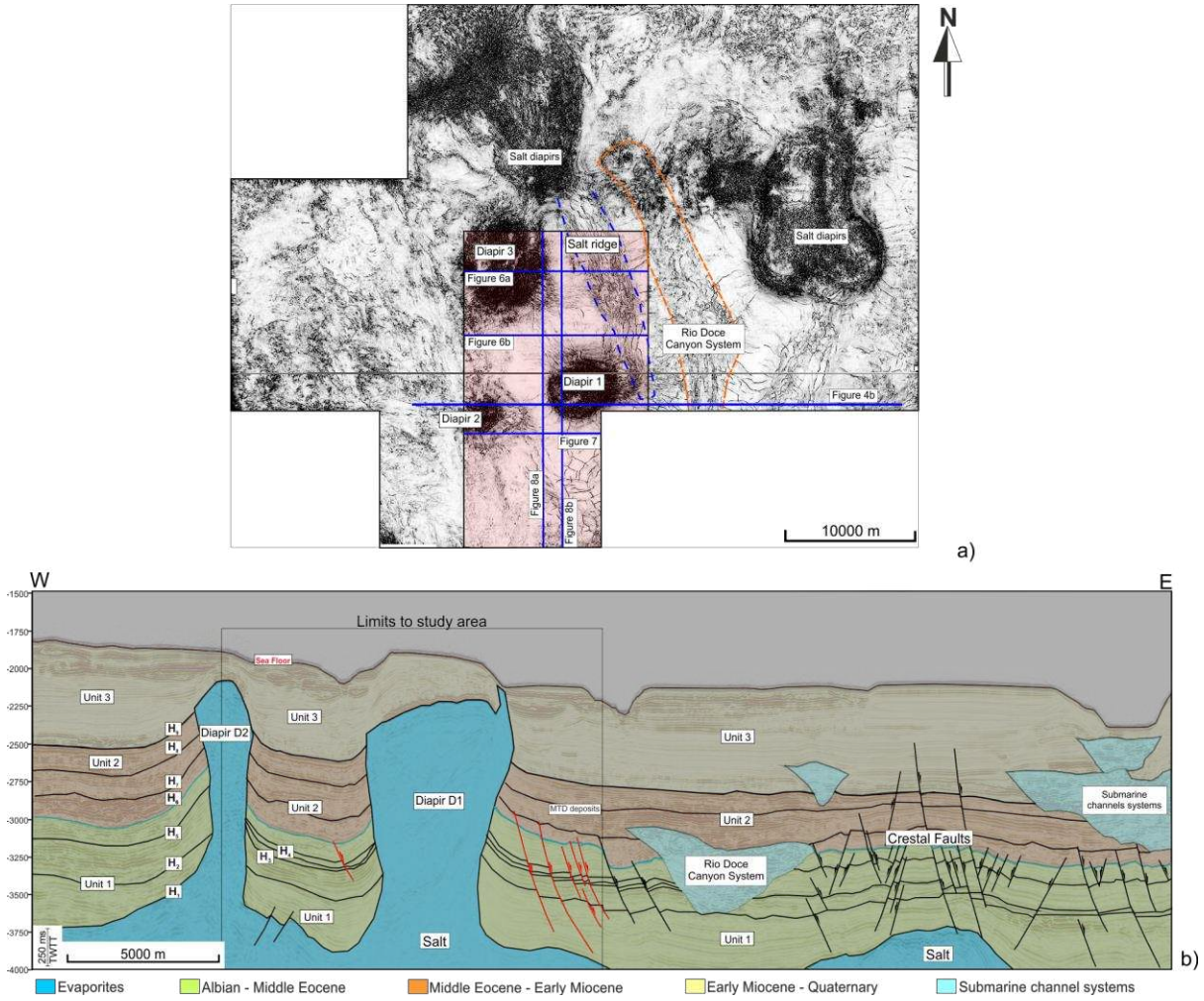

Figure 4: a) Variance time-slice at -3250 ms showing main geological features in the block BES-2. Salt diapirs and ridges are distinctive structures in this seismic cube. The Rio Doce Canyon System is delimited by the orange dashed line. The area of interest of this study is delimited by the red polygon. Three radially faulted salt diapirs and a faulted salt ridge are observed in the variance map. A large number of faults occur toward the southern half of the red polygon. b) Interpreted W-E regional seismic section of the Espírito Santo Basin showing main structures in the study area. The black polygon delimits the area of interest of this study and the faults adjacent to Diapir 2 are indicated in red. The blue line represents the Mid-Eocene unconformity (horizon H_6).

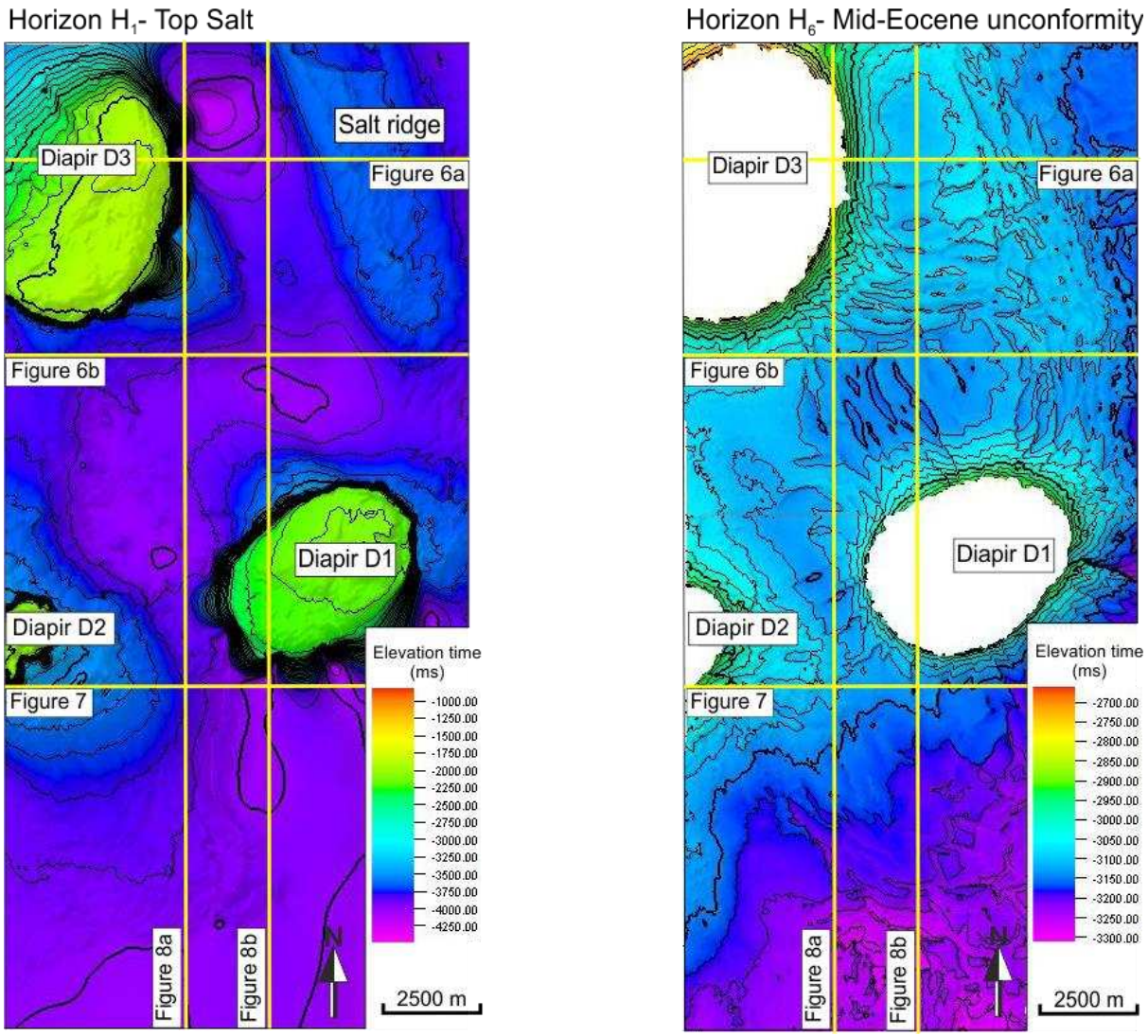

Figure 5: a) TWTT structural map of horizon H_1 highlighting the occurrence of salt diapirs and ridge in the study area. b) TWTT structural map of the regional Mid-Eocene unconformity (horizon H_6). Radial faults are observed adjacently to diapirs D2 and D3. However, these faults rarely propagate into Unit 2, which is delimited by horizon H_6 at its base.

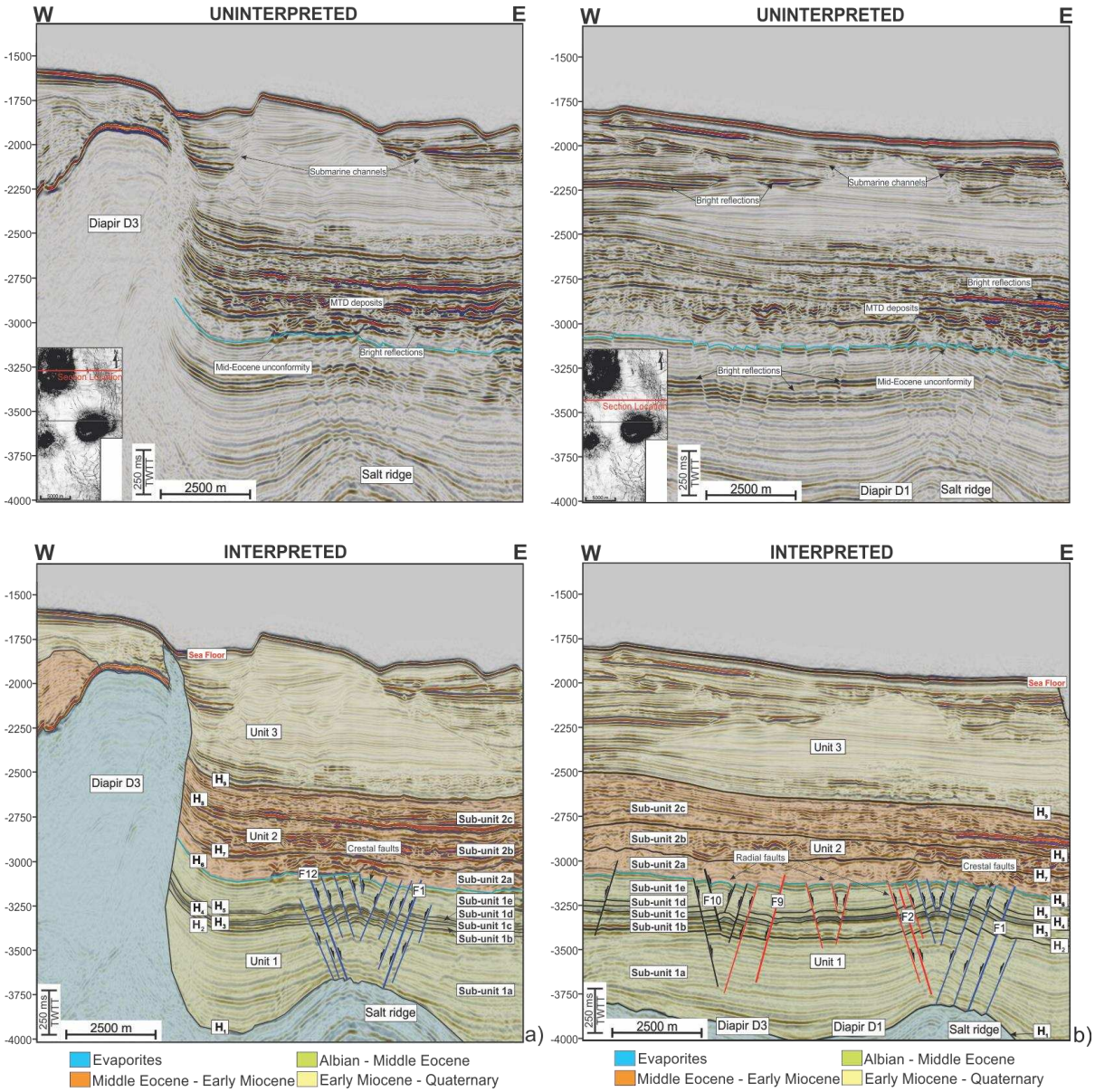

Figure 6: Sets of uninterpreted and interpreted W-E seismic sections. a) Seismic section crossing Diapir D3 and the Salt Ridge. Submarine channels are observed close to the seafloor and characterised by bright reflections. The interpreted seismic section highlights the presence of faults F1 and F12. Faults at the crest of the Salt Ridge comprise tilt blocks and terminate at horizon H_6, around which bright reflections are observed. Strata from Units 1 to 3 are deformed adjacent to diapir D3. b) Seismic section located between the salt structures highlighting the occurrence of bright reflections adjacent to D1 and D3 and the Salt Ridge. The interpreted seismic section shows that faults adjacent to D1 form tilt blocks with faults from the Salt Ridge and D3. Faults from D1 and D3 propagates into sub-unit 2a, whereas faults propagating from the Salt Ridge terminate at horizon H_6. Representative faults observed in this section include F1, F2, F9 and F10. The blue line represents the Mid-Eocene unconformity (horizon H_6).

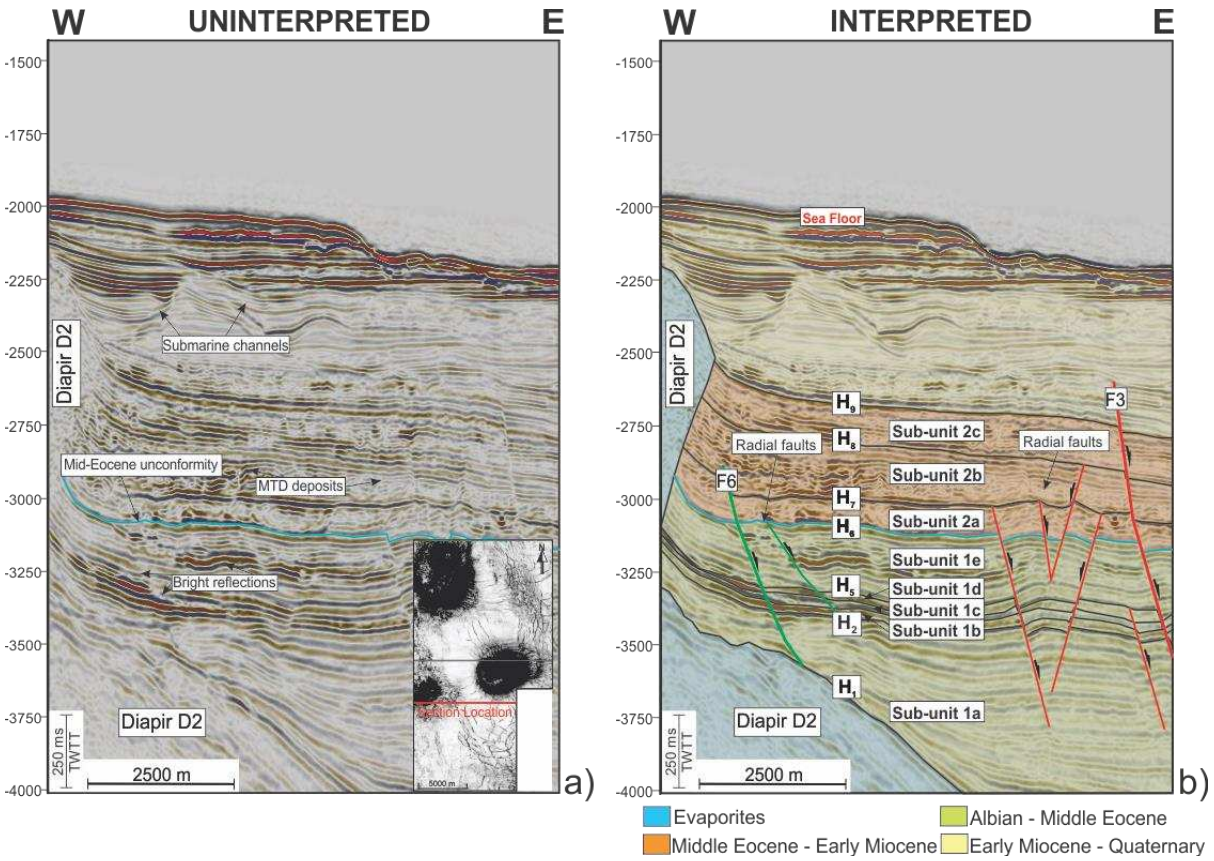

Figure 7: a) Uninterpreted W-E seismic line in the Espírito Santo Basin highlighting the occurrence of bright reflections close to diapir D2. Submarine channels are observed at a depth of -2500 ms below the sea floor. b) Interpreted seismic section showing that D2 deforms the three stratigraphic units. Representative faults in this region include faults F3 and F6. Fault F3 offsets Units 1 to 3, whereas fault F6 offsets Units 1 and 2. The blue line represents the Mid-Eocene unconformity (horizon H_6).

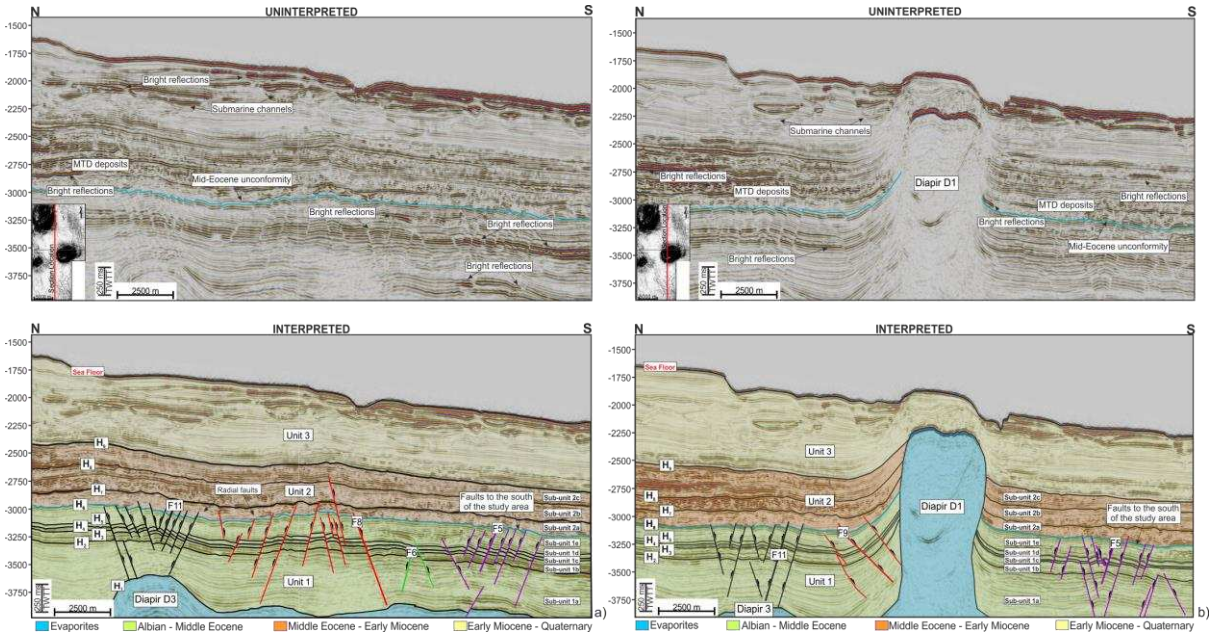

Figure 8: Uninterpreted and interpreted N-S seismic sections across the study area. a) Seismic section showing faults adjacent to diapirs D1, D2 and D3, and faults to the south of the study area. Bright reflections occur close to the sea floor, in Unit 2 to the north and in sub-units 1a to 1c for faults adjacent to D1 and D2 and to the south Faults adjacent to D1 and D3 offset Unit 2, whereas faults to the south are restricted to Unit 1. Representative faults observed in this section include F5, F6, F8 and F11. b) Seismic section showing that strata are deformed in the proximities of D1, and the radial character of the faults. Faults related to D3 and faults in the Southern Area form tilt blocks to the north and the south of this section, respectively. Representative faults observed in this section include F5, F9 and F11. The blue line represents the Mid-Eocene unconformity (horizon H_6).

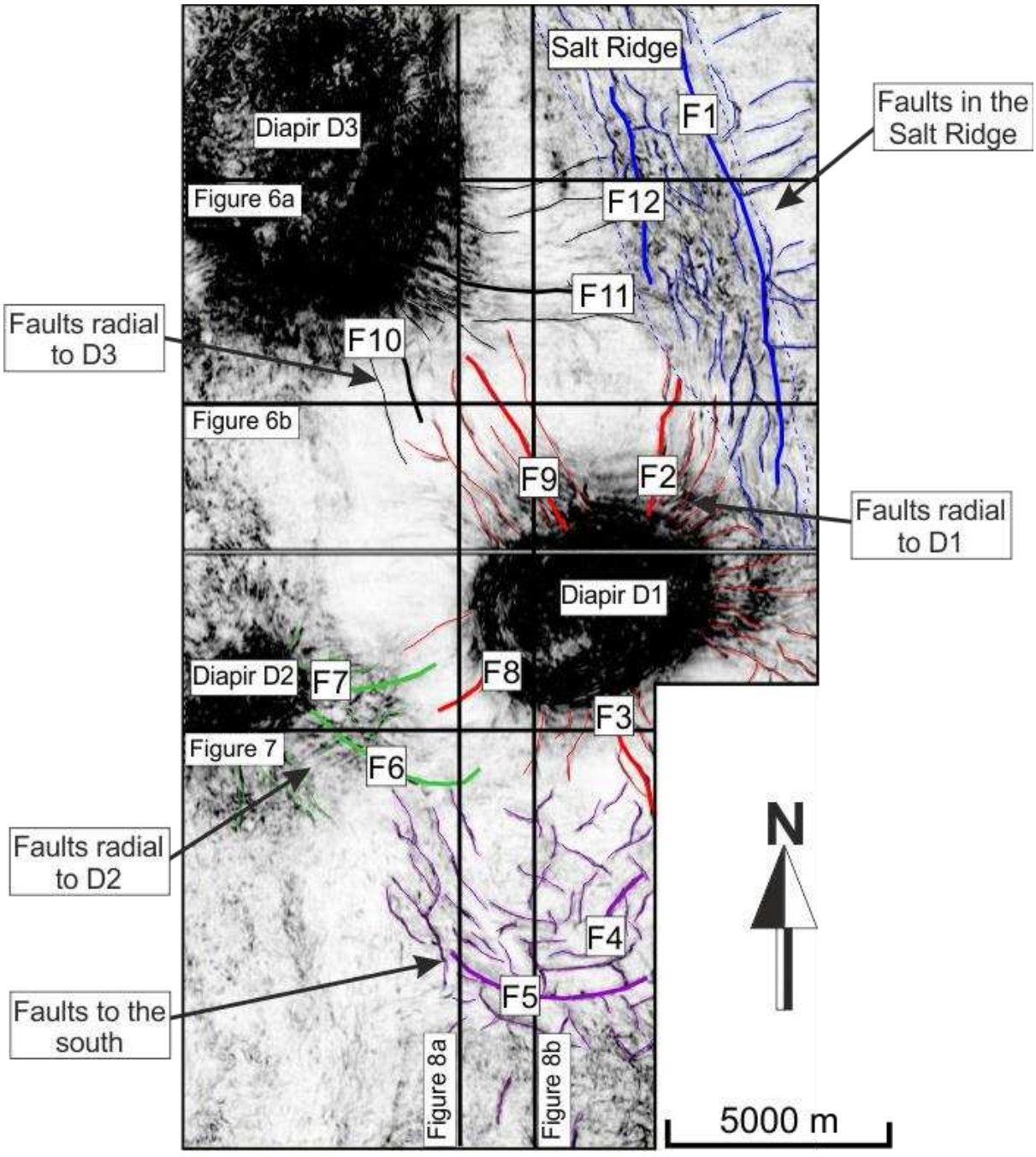

Figure 9: Variance time-slice at -3500 ms showing the locations of main fault families interpreted in the study area. Faults associated with the Salt Ridge are represented by the colour blue, whereas faults adjacent to D1 are in red. Faults to the south of the study area and adjacent to diapirs D2 and D3 are respectively shown in purple, green and black colours.

Salt Ridge

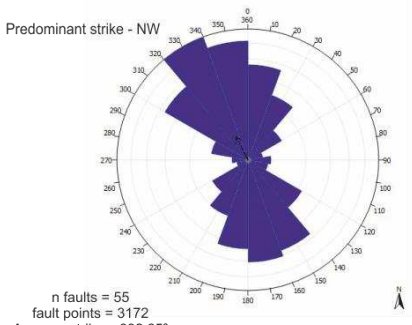

n faults = 55
fault points = 3172
Average strike = 332.65°

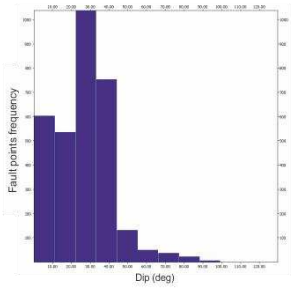

a)

Diapir D1

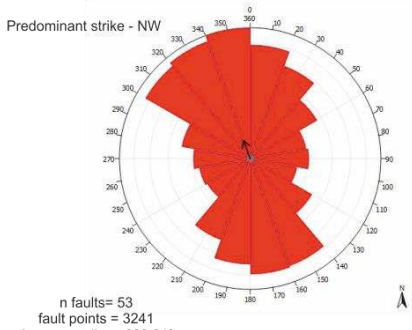

n faults= 53
fault points = 3241
Average strike = 339.91°

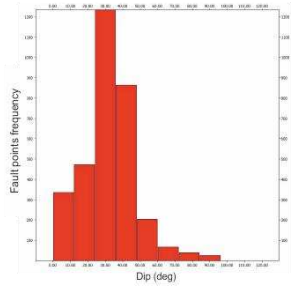

b)

South of the study area

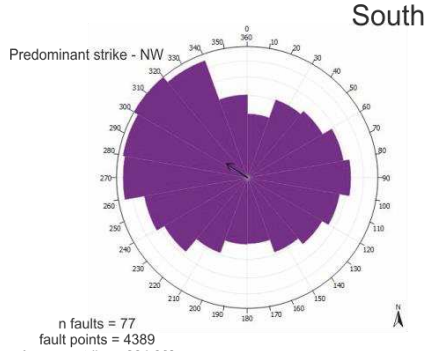

n faults = 77
fault points = 4389
Average strike = 304.00°

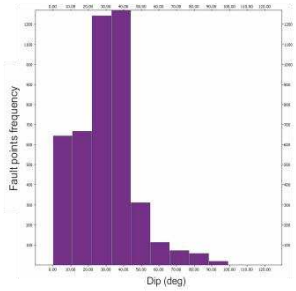

c)

Diapir D2

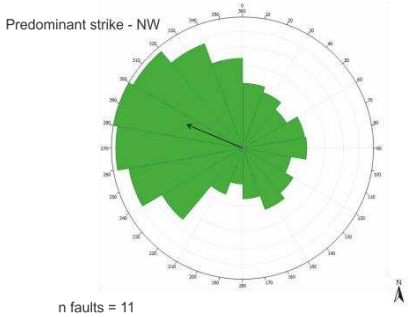

n faults = 11
fault points = 892
Average strike = 300.00°

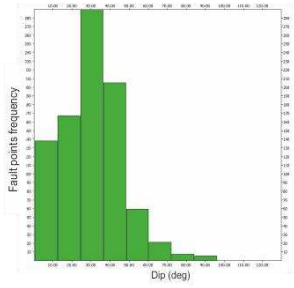

d)

Diapir D3

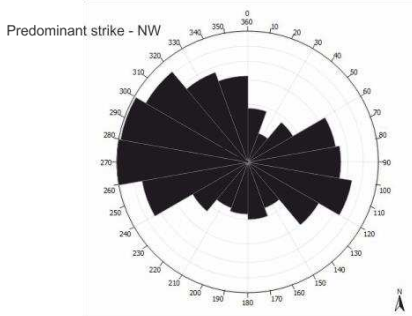

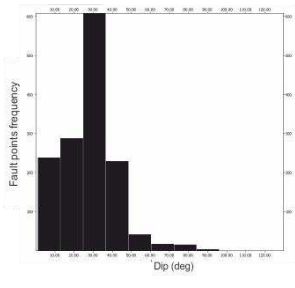

e)

Figure 10: Rose diagrams showing the strike and histograms showing the dip magnitude for the faults in the study area. Predominant strikes for the Salt Ridge are NW-SE and NE-SW. Faults close to D1 trend preferentially towards NW and NNE. In the south of the study area, faults are predominantly NW-SE and E-W. Faults predominantly strike to NW and SW close to D2. In diapir D3, faults show a predominant NW strike and a secondary SW strike.

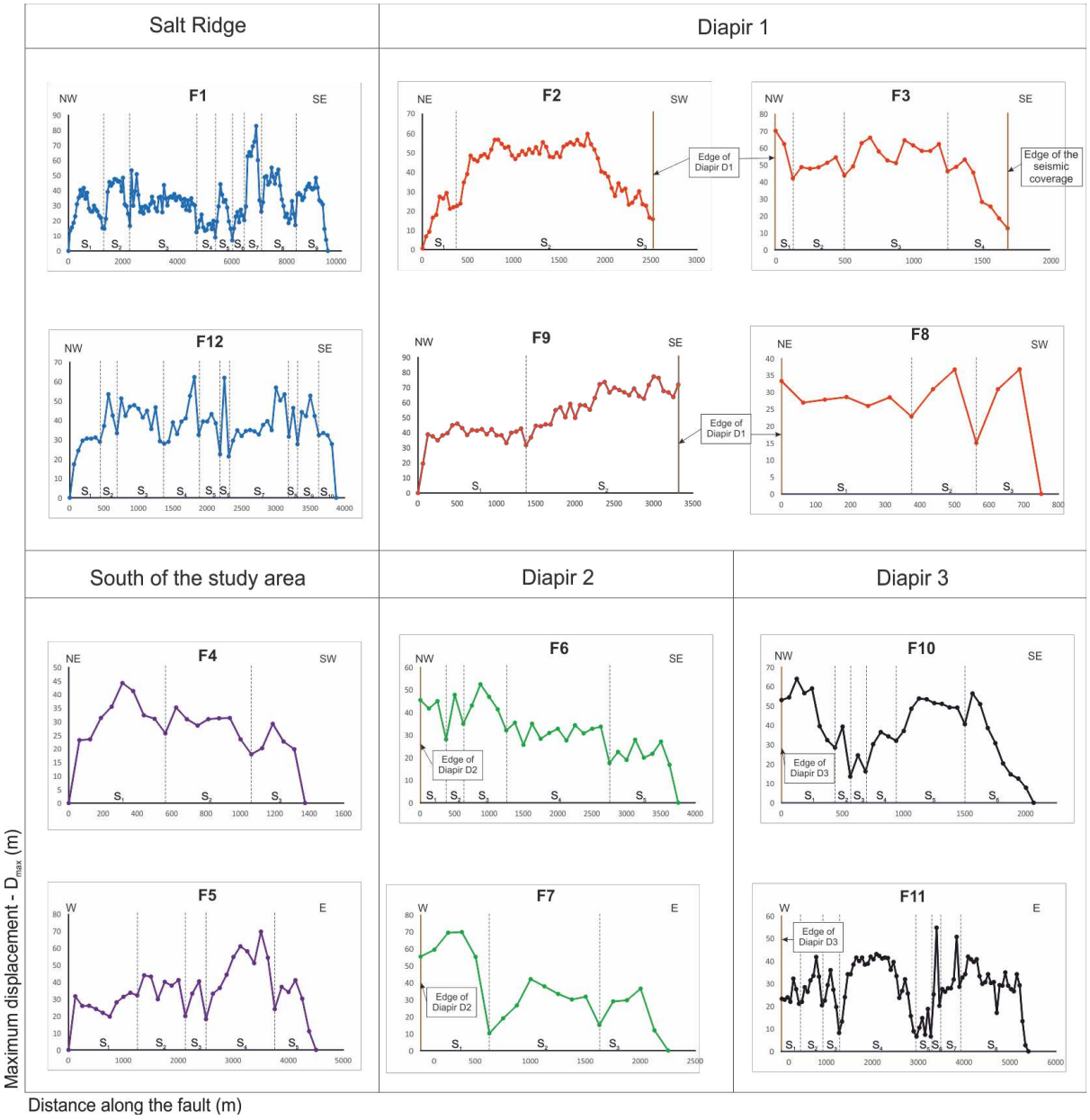

Figure 11: Displacement-length (D-x) plots for twelve representative faults. Faults are classified as C-type and M-type profiles based on Muraoka and Kamata (1983), as described in this work. Displacement curves were created along horizon H_5. Fault displacement and distance along the fault length are displayed in metres. Dotted lines and S1 to Sn denote distinct fault segments later linked to form a continuous fault plane.

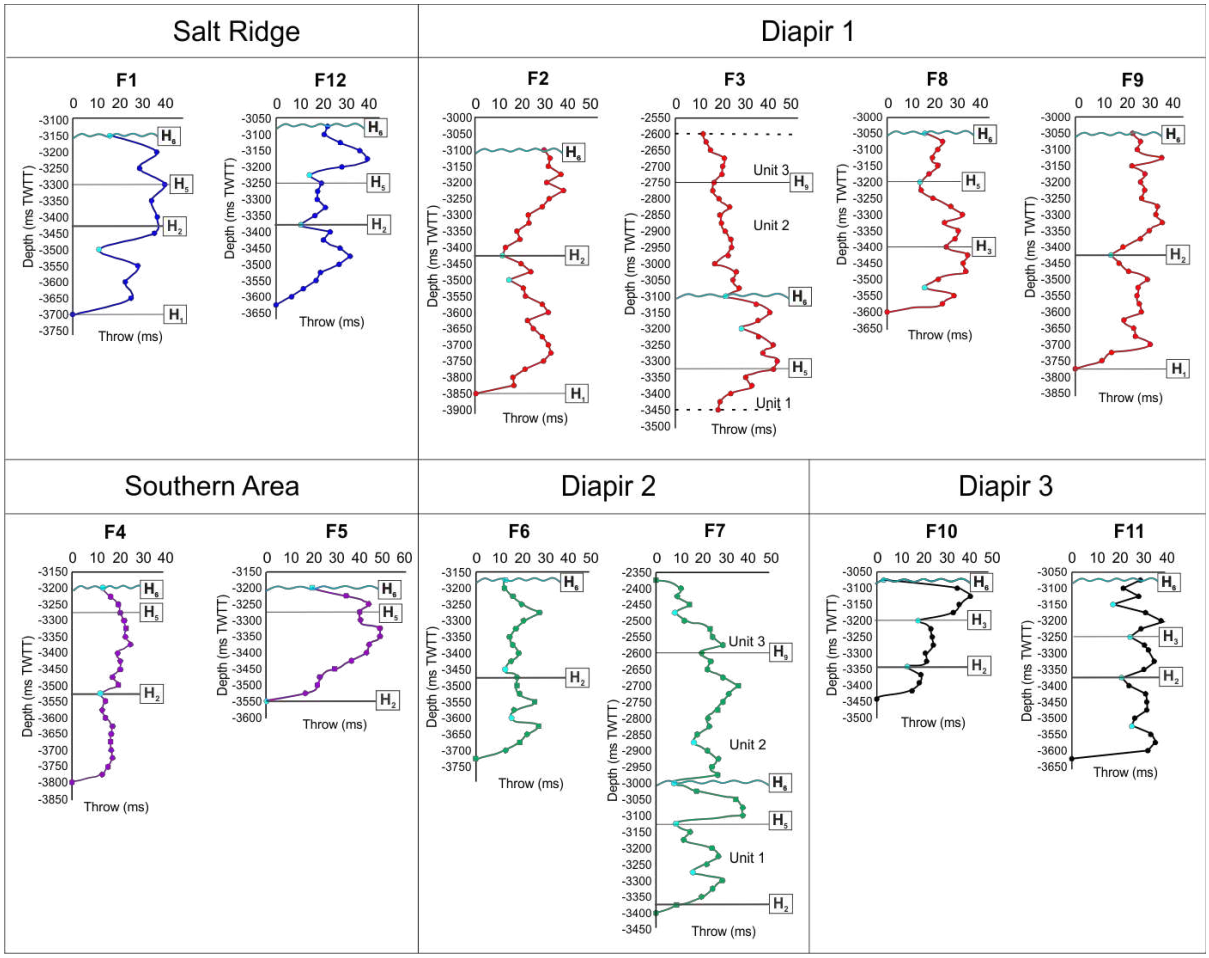

Figure 12: Throw-depth profiles for eight representative faults with both depth and throw measured in ms TWTT. Three throw profiles were identified based on these plots: asymmetric, M-type and skewed M-type. Grey lines indicate the horizons cut by the faults. The maximum throw for the majority of the faults occurs at horizon H_5. Throw minima are indicated by blue dots. The thick black line represents horizon H_2, where the first throw minima for most of the faults is recorded, whilst the blue line represents the Mid-Eocene unconformity (horizon H_6).

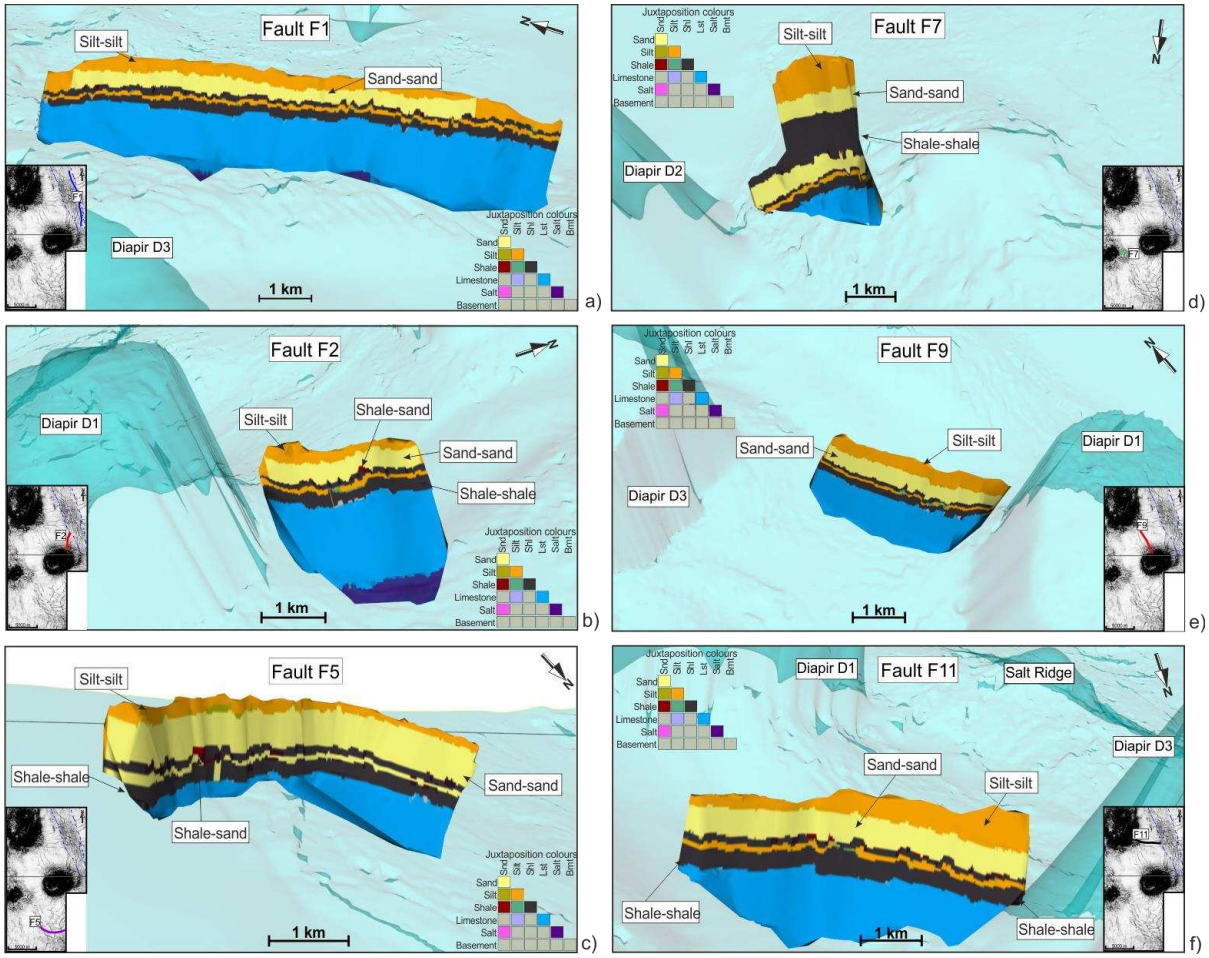

Figure 13: Juxtaposition diagrams for representative faults in the study area. a) Fault F1 showing juxtaposed sand units in its central part and a permeable interval defined by a shale interval. Close to the fault terminations juxtaposed limestone and sand-shale and sand-silt contacts are observed. b) Fault F2 showing sand units delimited vertically and laterally by impermeable units. c) Juxtaposition diagram for fault F5 showing an upper sand body laterally delimited by contacting silt units to W. d) Fault F7, showing that juxtaposed sand bodies are delimited vertically by a thin shale layer close to Diapir D2 e) Fault F9 showing a sand body isolated by a sit-silt juxtaposition at the NW and SE terminations. f) Fault 11 showing the sand-sand contact delimited vertically by a silt-silt juxtaposition that increases in thickness towards the Diapir D3. The diagrams use a colour code chart to indicate the degree of juxtaposition between distinct units. Superimposed shale units are indicated in brown along the fault trace, whereas sand juxtaposition is defined in yellow.

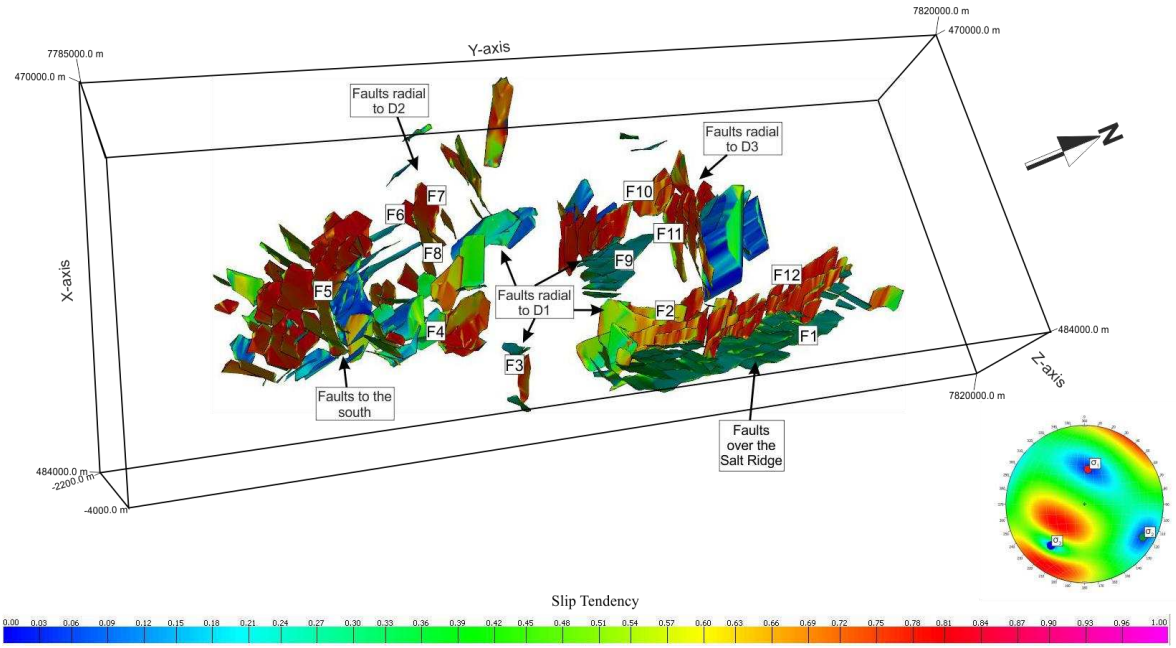

Figure 14: Slip tendency model for faults in the study area considering the paleostress tensor for the faults over the Salt Ridge. Slip tendency values range from 0.03 to 0.82, with an average of 0.53. Faults striking to NW show larger slip tendency values than faults striking to NE.

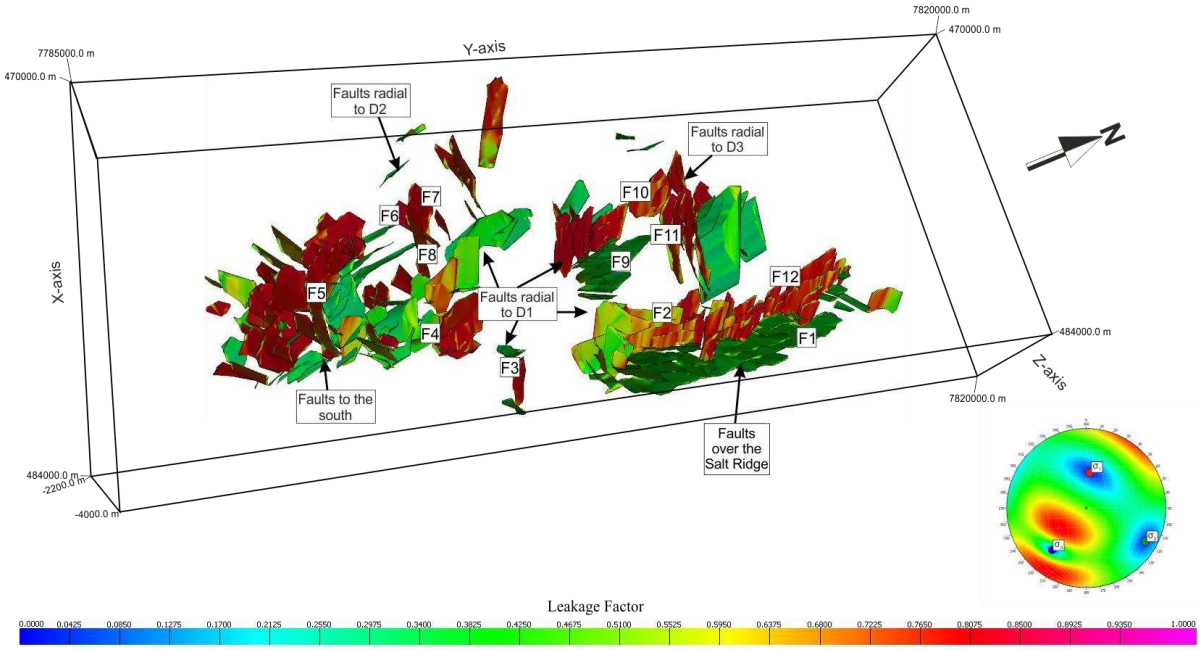

Figure 15: Leakage Factor model for faults in the study area considering the paleostress tensor for the faults over the Salt Ridge and a fluid pressure of 9 MPa. Leakage factors for the study area range from 0.27 to 0.85.

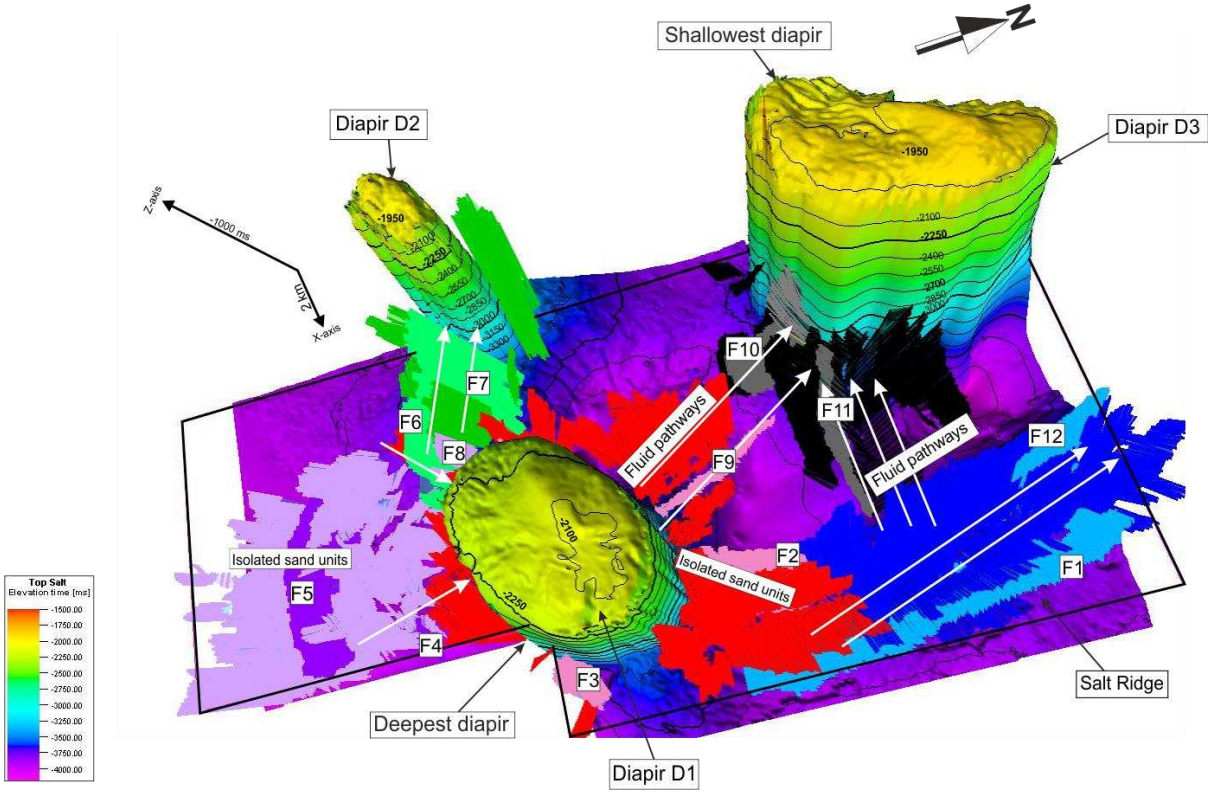

Figure 16: 3D representation of faults associated with halokinesis in the study area. The white arrows indicate a preferential fluid flow direction based on the leakage factor and juxtaposition analysis from south to north-northwest, in direction to D3. Isolated sand units were found in the vicinity of fault F2, adjacent to D1, and fault F5, in the southern part of the study area.